Journal of Structural Dynamics, 4, (pp. 1-24) 2025
Exciter Force Control for Vibration Testing of Nonlinear Structures Using Adaptive Feedforward Cancellation

Journal of
Structural
Dynamics

Exciter Force Control for Vibration Testing of Nonlinear Structures Using Adaptive Feedforward Cancellation

Nikola Ristic *[1], Ibrahim A. Sever †[2], and Ludovic Renson ‡[1]

[1] *Imperial College London, Mechanical Engineering Department, Exhibition Rd, London, SW7 2AZ, UK*
[2] *Rolls-Royce plc, SinA-33, PO Box 31, Derby, DE24 8BJ, UK*

Abstract

Vibration testing of nonlinear structures presents various challenges that are not only related to the nonlinear structure itself but also to the exciter. As the exciter and the structure are coupled, the structure's nonlinear behaviour distorts the exciter force amplitude and frequency content, making the test results more difficult to compare with numerical predictions or even less accurate when isolating and identifying nonlinear normal modes (NNMs). This paper uses an adaptive feedforward cancellation (AFC) real-time control algorithm to track multi-harmonic force reference signals accurately. The controller estimates the disturbance generated by the structure and adjusts the exciter's input to compensate for it, recovering the desired force signal. The advantage of this approach is that it does not rely on the knowledge of the exciter and structure models. It only requires knowledge of the phase at the output of the exciter, which is straightforward to estimate experimentally from the force measurements. The effectiveness of the AFC for exciter force control is demonstrated numerically and experimentally on a cantilever beam structure excited by an electromagnetic shaker.

The beam's free tip is attached to a spring mechanism, giving rise to geometric nonlinearities and mode interactions resulting in strong harmonic distortions in the excitation force. The method is further demonstrated on a compressor blade from Roll-Royce's aero-engine.

Keywords: Force Control; Nonlinear Vibration

Received on August 20, 2025, *Accepted on November 13, 2025*, *Published on November 17, 2025*

1 Introduction

Experimentally achieving a specific input force using an electrodynamic shaker can be challenging, even for a linear structure, as the shaker and the structure dynamically interact near the structure's resonance, leading to the well-known force drop-out phenomenon [1, 2]. This problem is compounded for nonlinear structures where higher-harmonics in the structure's response are reflected back to the shaker, distorting the input force profile [3]. The harmonic distortion of the force can even originate from the nonlinearities of the exciter itself [4]. These exciter-structure interactions are often overlooked during experimental testing, even though they can significantly impact the accuracy of the results [3]. For instance, this means that each periodic response is measured at a slightly different forcing level, which can lead to seemingly noisy frequency response data. The force distortion also plays a significant role for the nonlinear force appropriation [5], where the harmonic content of the excitation force needs to be carefully chosen in order to isolate a nonlinear normal mode of the structure. This entails that the phase quadrature is achieved for each harmonic present in the response of the structure [6]. Precise control of the force signal is also essential for High Cycle Fatigue

---

*`nr320@ic.ac.uk`
†`Ibrahim.Sever@Rolls-Royce.com`
‡`l.renson@imperial.ac.uk`

assessment, where poor force control can result in poor repeatability in achieved stress amplitudes and a lack of consistency between tests, ultimately resulting in lengthy and costly experimental campaigns.

This paper presents a simple control method that can achieve a desired multi-harmonic input force on a nonlinear structure, overcoming the force drop-out and harmonic distortion issues without the need for a model of the structure and limited knowledge about the exciter dynamics. Specifically, for improved performance and stability, the method requires identifying the phase between the input voltage and excitation force, which can be obtained using standard testing and linear identification methods.

Exciter control is commonly used for achieving specific acceleration profiles (e.g. [7, 8]), relying on the knowledge of a linear exciter model, as well as its electro-mechanical parameters. A similar approach, exploiting the knowledge of a linear model, was later adopted to control the force of the exciter [9]. This linear control approach is based on the inversion of the exciter model, which assumes that the model perfectly captures the dynamics of the exciter. This approach can be unsuccessful if the exciter parameters are not accurately determined or if there are slight variations in the dynamics of the exciter, which can occur when coupled to a nonlinear structure. Furthermore, because the reference signal is sinusoidal rather than constant, the controller cannot entirely eliminate the steady-state error. This shortcoming stems from the fact that its transfer function lacks an internal model of the reference/disturbance. The internal model principle (IMP) asserts that to achieve zero steady-state error, a controller must incorporate dynamics capable of generating the reference/disturbance signal itself [10]. A controller of the form presented in [9] will also typically produce a lag with respect to the reference signal as the excitation frequency increases, because the phase characteristic of the system cannot always be designed to be at 0° at the frequency range of interest. An improved approach, which considers exciter parameter uncertainties, is investigated in [11], although at the expense of a more complicated iterative design procedure, which results in a high-order controller transfer function. In [11], the effect of the structure on the exciter is formulated as a disturbance that should be rejected by the controller. This disturbance is estimated based on the measurements of the exciter coil current and the structure's acceleration and displacement. Measurements of the structure's velocity are also used within the control loop. While this approach takes into account possible variation of the plant parameters during nonlinear structure testing, it requires many states of the coupled exciter-structure system to be measured, which can be expensive and impractical. Additionally, as in the approach of [9], it is designed for the regulation of a constant reference value. Hence, it cannot systematically remove the steady-state error when tracking a sinusoidal signal.

To correct for harmonic distortions of the force, Josefsson et al. [12] presented an approach based on least squares estimation. The measured force signal is parametrised based on the assumption that it is a sum of sinusoidal basis functions. The error with a reference signal is then iteratively minimized using Newton-Raphson/Broyden methods, introducing higher-harmonics in the voltage to compensate for those in the force. The method was experimentally demonstrated in [13]. While this approach can systematically deal with higher harmonics, it has multiple drawbacks. As the scheme is iterative, it has to be performed offline on multiple (buffered) measurement points. Execution of the numerical algorithms is slow and requires derivatives of noisy data, which makes it prone to failure (as observed in [14]). A similar approach was developed for audio applications in [15] and later demonstrated on an electro-magnetic vibration exciter. As in [12], the signal was parametrized by sinusoidal basis functions. The frequency response function (FRF) of the exciter is estimated beforehand and its inverse is used to estimate the appropriate correction. Fourier coefficients of estimated harmonics are then fed to the input voltage to produce a single-harmonic force. The disadvantage of this approach is that it relies on a predetermined exciter FRF, while not considering possible uncertainties in the parameters or the model structure. Additionally, both of the methods above require signal buffering, which can result in a slow force correction process. More recently, real-time exciter force control was achieved by assuming that the signal can be represented as a Fourier series and applying proportional control on the amplitude rather than the force measurement signal [16]. Applying control to the amplitude can eliminate the steady-state error, but only if an integral term is included. The assumption that there is no phase difference between the input voltage and the force was also made. This approach can perform well in a limited frequency range, where this assumption is satisfied. This range is in the vicinity of the phase resonance of the structure, where the applied force will be in phase with its velocity and hence with the input voltage. In [17], Hippold et al. estimate the Fourier coefficients of higher harmonics present in the response by a least mean squares (LMS) filter and apply proportional-integral (PI) control to each coefficient. The authors show that if the real part of the linearized frequency response of the shaker-structure system is greater than 0, the closed-loop system is stable. This is known as the strict positive real (SPR) condition [18].

In the present paper, we view the exciter force control problem as a disturbance rejection problem that can be addressed through the adaptive feed-forward cancellation (AFC) algorithm, whilst still exploiting the Fourier series representation of the excitation signal. AFC is often used for noise suppression in audio applications [19] and has also proven very successful in controlling hard-drive disks [20], where similar harmonic distortion problems are encountered. Similar to some approaches found in the literature, AFC estimates the Fourier coefficients of the disturbance acting on the force, which originates from the unknown nonlinear structure. In contrast to [17], AFC provides a unified methodology, where estimation and control action are not decoupled. Sacks et al. [20] also show that the SPR-like condition needs to be satisfied only at the frequencies of interest. With knowledge of the exciter phase, a particular advantage of AFC is that the stability requirements are relaxed further and relatively large gain and phase stability margins are obtained, such that, in practice, no knowledge of the exciter and structure models, or their parameters, is needed (see Section 2.3). The proposed methodology can be applied to base excitation without any adjustments, other than measuring acceleration instead of force, following the same principles outlined in [17].

The AFC method is first demonstrated on an academic structure consisting of an electrodynamic shaker attached to a cantilever beam with a nonlinearity attached at its free end, giving rise to geometric nonlinearity. The structure is tuned to exhibit a 3:1 modal interaction between its first two bending modes, leading to an isolated response as in [14]. In the interaction region, the responses exhibit high harmonic distortions strongly affecting the force, which creates a suitable setting for a practical evaluation of the force controller performance. The method is then demonstrated on an industrial component – a compressor blade from Rolls-Royce's aero-engine.

The developed control algorithm is here demonstrated in the context of standard stepped sine and sine sweep tests. However, it could also be used alongside recent control-based testing methods, such as response-controlled stepped sine testing (RCT) [21], phase-locked loop (PLL) testing [22, 6, 23, 24, 25, 26] and control-based continuation (CBC) [27, 28, 29, 30, 31, 32, 33, 34], that were specifically developed for characterising nonlinear vibrations. These methods employ a stabilizing controller that allows the unstable responses to be reached during the experiment, providing a systematic and robust methodology for identifying frequency response and backbone curves.

The structure of this paper is as follows. Section 2 presents the adaptive AFC method used to control the force of the exciter. Simulations on a model of the exciter-beam system are then presented in Section 3. The performance of the controller is then evaluated experimentally on the shaker-beam system in Section 4, and on the shaker-blade system in Section 5. Finally, some concluding remarks and potential future applications are given in Section 6.

2 Exciter Force Control

2.1 Exciter Reference Force Tracking and Disturbance Rejection

An exciter-structure system usually consists of electrical and mechanical parts, where the coupling between those parts can lead to force distortion. In order to simplify the controller design, the distortion is represented as an external disturbance acting on the exciter. This assumption is made possible by the fact that the disturbance coming from the structure can be represented as a truncated Fourier series. Such an approach avoids the direct inclusion of an unknown nonlinear structure in the design of the exciter force controller. The disturbance rejection problem can thus be formulated as:

$$\begin{aligned} \dot{\mathbf{x}}_\mathbf{e} &= \mathbf{f}(\mathbf{x}_\mathbf{e}) + \mathbf{B}(u - d), \\ y &= \mathbf{g}(\mathbf{x}_\mathbf{e}) = F, \end{aligned} \tag{2.1}$$

where $u = u(t)$ is the input voltage (control signal), $\mathbf{x}_\mathbf{e}$ is the state vector of the exciter (e. g. displacement, velocity, current), $\mathbf{f}$ is the function that describes the exciter dynamics, $\mathbf{B}$ is the input gain, $y = \mathbf{g}(\mathbf{x}_\mathbf{e}) = F$ is the output force and $d = d(t)$ is the disturbance to be rejected. The disturbance is also assumed to be independent of the structure dynamics. This assumption is obviously incorrect, but still reasonable if the dynamics of the structure is faster than the controller dynamics. The simplification of the control problem is illustrated in Figure 1 using block diagrams.

2.2 Adaptive feed-forward Cancellation

Adaptive feed-forward cancellation (AFC) operates on the premise that if the harmonic disturbance was known, it could simply be compensated for by including it in the control signal. Since the disturbance is usually unknown, it needs to be estimated. This idea originated independently in various fields and is sometimes referred to as Modulated-demodulated control [35, 36, 37] or simply as adaptive notch filters [38, 39].

A typical AFC control architecture for tracking a harmonic reference signal $r(t)$, and rejecting a harmonic disturbance $d(t) = a\cos\omega t + b\sin\omega t$, is shown in Figure 2. $P(s)$ represents the transfer function of the plant (i.e. from the input voltage to the output force), and $\frac{1}{s}$ represents the transfer function of the integral action in the Laplace domain. It should be noted that $P(s)$ is not truly the transfer function of the exciter, as it will still encompass some contribution

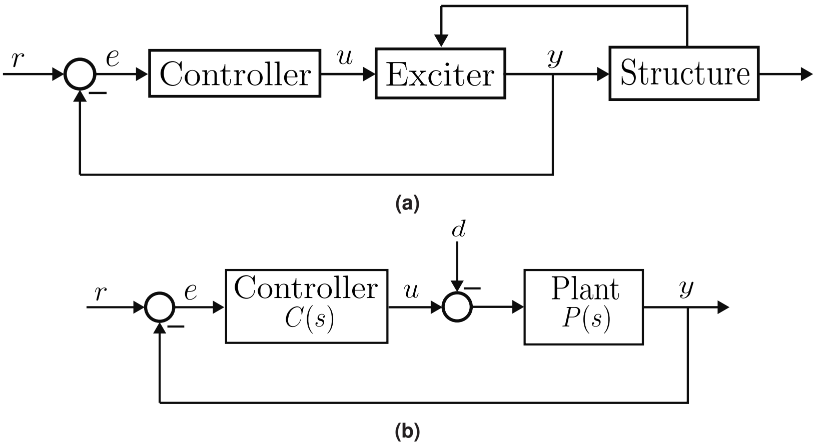

Fig. 1: (a) Block diagram of the full exciter-structure-controller system; (b) Block diagram of the simplified plant-controller system with external disturbance

from the structure itself. The Fourier coefficients, a and b, of the disturbance, $d(t)$, are estimated and subsequently minimized using:

$$\begin{aligned} \dot{\hat{a}}(t) &= 2Ke(t)\cos(\omega t + \phi), \\ \dot{\hat{b}}(t) &= 2Ke(t)\sin(\omega t + \phi), \end{aligned} \tag{2.2}$$

where ω is the disturbance frequency, ϕ is a phase parameter and $\hat{a},\ \hat{b}$ are estimates of the true Fourier coefficients $a,\ b$ of the disturbance. The disturbance frequency is assumed to be known as it corresponds to the excitation frequency or one of its harmonics. Estimation of the Fourier coefficients can be performed by different algorithms, including standard demodulation (as in Figure 2) or more sophisticated filters like recursive least squares [40] or Kalman filter [41], if required. The fundamental Fourier coefficients of the tracking error are subsequently modulated by harmonic signals and fed back to the plant.

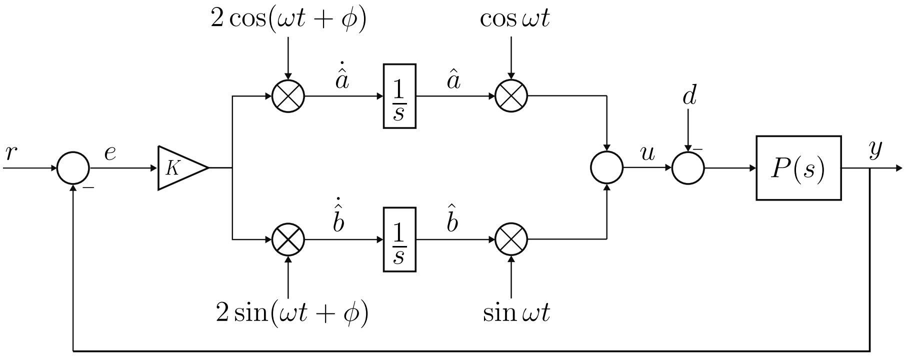

Fig. 2: AFC with the phase parameter

This approach can be expanded to address multiple harmonics by simply having multiple AFC loops connected in parallel. Each AFC loop allows tracking/rejection of one specific frequency. In this way, a reference signal is successfully tracked, preventing the force drop-out and rejecting higher-harmonic disturbances generated by any nonlinear periodic behaviour. Convergence of the steady-state error to zero is achieved regardless of the plant's dynamics, as shown in Appendix C. If there is a significant DC offset produced by the sensor, an additional integral loop can be added to remove it [42]. In this way, a disturbance generated by a nonlinear system can be successfully compensated by a linear (but adaptive) control law.

The advantage of AFC is that it is applicable to different vibration exciters, as it does not rely on any modelling of the exciter and structure. Even if a nonlinearity is present in the exciter, the method will still provide good performance, assuming the exciter is open-loop stable. The reason for this is that the dynamics of such exciters can be locally approximated by a linear system, as long as any changes in the exciter dynamics occur slowly. The last assumption can be assumed valid in the context of stepped sine testing and sufficiently slow sine sweeps, as illustrated in Sections 3–5.

2.3 Improving the Stability Margins and Transient Performance of AFC

To assess the transient performance and stability of the closed-loop system with the AFC controller, averaging analysis based on [43] is conducted. In order to apply the averaging method, it is assumed that the plant open-loop transfer function, $P(s)$, is stable [43], which is true for electrodynamic shakers. The structure dynamics is ignored in this analysis and is only considered as an external disturbance.
From Figure 2, the closed-loop system dynamics can be written as:

$$\dot{\mathbf{x}} = \mathbf{A}\mathbf{x} + \mathbf{B}(u-d), \tag{2.3}$$

$$y = \mathbf{C}\mathbf{x}, \tag{2.4}$$

$$u - d = \boldsymbol{\varphi}^T\boldsymbol{\theta}, \tag{2.5}$$

$$\dot{\boldsymbol{\theta}} = 2K\boldsymbol{\varphi}'(r-y), \tag{2.6}$$

$$\boldsymbol{\theta} = \left[\hat{a} - a \;\; \hat{b} - b\right]^T, \tag{2.7}$$

$$\boldsymbol{\varphi} = [\cos\omega t \;\; \sin\omega t]^T, \tag{2.8}$$

$$\boldsymbol{\varphi}' = [\cos(\omega t + \phi) \;\; \sin(\omega t + \phi)]^T, \tag{2.9}$$

where $\mathbf{A}$, $\mathbf{B}$ and $\mathbf{C}$ are the state, input and output matrices associated with the state space representation of $P(s)$. Using the state equation (2.3) and the output equation (2.4), the output of the system can be expressed in terms of its transfer function:

$$y = \mathbf{C}\,(sI - \mathbf{A})^{-1}\,\mathbf{B}[u-d] = P(s)[u-d] = P(s)\left[\boldsymbol{\varphi}^T\boldsymbol{\theta}\right]. \tag{2.10}$$

Inserting (2.10) into (2.6) now gives

$$\dot{\boldsymbol{\theta}} = 2K\boldsymbol{\varphi}'\left(r - P(s)\left[\boldsymbol{\varphi}^T\boldsymbol{\theta}\right]\right). \tag{2.11}$$

Assuming that the parameters are updated on a slower time scale than the process (fast oscillations of the vibrating structure/exciter) time scale, the following expression can be obtained [43]:

$$\dot{\bar{\boldsymbol{\theta}}} = -2K\bar{\mathbf{z}}\bar{\boldsymbol{\theta}}, \tag{2.12}$$

where $\mathbf{z} = \left(\boldsymbol{\varphi}' P(s)\left[\boldsymbol{\varphi}^T\right]\right)$ and $\bar{(\cdot)} = \lim_{T\to\infty}\frac{1}{T}\int_0^T (\cdot)dt$ is the averaging operation. The fact that the average of $\left(\boldsymbol{\varphi}' P(s)\left[\boldsymbol{\varphi}^T\boldsymbol{\theta}\right]\right)$ is equal to the average of $\left(\boldsymbol{\varphi}' P(s)\left[\boldsymbol{\varphi}^T\right]\right)\bar{\boldsymbol{\theta}}$ in equation (2.12), is a consequence of the assumption that the variation of the parameters is much slower than the dynamics of the plant and can be considered constant during the averaging period. This is ensured by choosing a sufficiently small gain K. The reference, r, is considered to be 0 in order to simplify the derivations, as it has no effect on the average dynamics. The details of the averaging procedure are given in Appendix A.
Following the averaging procedure, the averaged error dynamics is [20]:

$$\dot{\bar{\boldsymbol{\theta}}} = -K\begin{bmatrix} Re\{P(j\omega)\}\cos\phi + Im\{P(j\omega)\}\sin\phi & -Re\{P(j\omega)\}\sin\phi + Im\{P(j\omega)\cos\phi \\ Re\{P(j\omega)\}\sin\phi - Im\{P(j\omega)\}\cos\phi & Re\{P(j\omega)\}\cos\phi + Im\{P(j\omega)\}\sin\phi \end{bmatrix}\bar{\boldsymbol{\theta}}, \tag{2.13}$$

where $P(j\omega) = P(s)|_{s=j\omega}$.
The eigenvalues of the averaged system (2.13) are:

$$\begin{aligned}\lambda_{1,2} = & -K\,(Re\{P(j\omega)\}\cos\phi + Im\{P(j\omega)\}\sin\phi \\ & \pm j\,(Re\{P(j\omega)\}\sin\phi - Im\{P(j\omega)\}\cos\phi)),\end{aligned} \tag{2.14}$$

Considering that $Re\{P(j\omega)\} = |P(j\omega)|\cos\phi_p$ and $Im\{P(j\omega)\} = |P(j\omega)|\sin\phi_p$, choosing the phase parameter ϕ such that $\phi = \phi_p$ will eliminate the imaginary part of the eigenvalues and lead to faster convergence with the eigenvalues [20]:

$$\lambda_{1,2} = -K\,|P(j\omega)|. \tag{2.15}$$

It can be observed from (2.14) that the real part of the eigenvalues can become positive, and thus lead to instability, if ϕ is chosen too far from ϕ_p.

Setting the phase parameter to the phase of the plant is expected to provide a large phase margin, leading to improved stability properties [44]. This can be shown from the LTI transfer function representation of the controller (B9) derived in Appendix B:

$$C(s) = 2K\frac{s\cos\phi + \omega\sin\phi}{s^2+\omega^2} = 2K\frac{D(s)}{Q(s)}. \tag{2.16}$$

The phase of the controller transfer function is then given by:

$$\operatorname{Arg}\{C(j\omega)\} = \operatorname{Arg}\{D(j\omega)\} - \operatorname{Arg}\{Q(j\omega)\}. \tag{2.17}$$

The argument of the transfer function numerator is given by:

$$D(j\omega) = j\omega\cos\phi + \omega\sin\phi = j\omega(\cos\phi - j\sin\phi) = j\omega e^{-j\phi} = \omega e^{j\frac{\pi}{2}}e^{-j\phi} = \omega e^{j\left(\frac{\pi}{2}-\phi\right)}, \tag{2.18}$$

$$\operatorname{Arg}\{D(j\omega)\} = \frac{\pi}{2} - \phi. \tag{2.19}$$

Following [44], the argument of the transfer function denominator is discontinuous, and changes from 0 to $-\pi$ at the reference frequency. Its average value is defined to be:

$$\operatorname{Arg}\{Q(j\omega)\} = \frac{\operatorname{Arg}\{Q(j\omega^-)\} + \operatorname{Arg}\{Q(j\omega^+)\}}{2} = \frac{0-\pi}{2} = -\frac{\pi}{2}. \tag{2.20}$$

Substituting (2.19) and (2.20) into (2.17) gives the phase of the controller:

$$\operatorname{Arg}\{C(j\omega)\} = \frac{\pi}{2} - \phi - \frac{\pi}{2} = -\phi. \tag{2.21}$$

The phase of the open-loop transfer function $W_{ol}(s) = C(s)P(s)$ is given by the following expression:

$$\operatorname{Arg}\{W_{ol}(j\omega)\} = \operatorname{Arg}\{C(j\omega)\} + \operatorname{Arg}\{P(j\omega)\} = -\phi + \operatorname{Arg}\{P(j\omega)\} = -\phi + \phi_p. \tag{2.22}$$

It is clear that setting the phase parameter to $\phi = \phi_p$ is expected to provide a large phase margin because the discontinuous phase jump in $W_{ol}(j\omega)$ will always be centered around $0°$ and transition from $90°$ to $-90°$, as can be seen from Figure 3. This results in close to $90°$ phase margin regardless of the reference/disturbance frequency, i.e. the system will be stable as long as the actual phase does not differ from the one used in the controller by more than $90°$. The plant model used in Figure 3 is an electrodynamic shaker coil of the form $L\dot{I} + RI = u$. The parameters used for the model are given in Section 3. Figure 3 shows that the phase of $W_{ol}(j\omega)$ with $\phi = 0$ is identical to the phase of $P(j\omega)$ at the reference/disturbance frequency (chosen equal to 1kHz in Figure 3). With $\phi = \phi_p$, the phase of $W_{ol}(j\omega)$ is recentered at $0°$, increasing the phase margin.

It should be noted that the phase does not necessarily need to be obtained from the plant model, as it can be estimated from the measurements of the output using standard FRF estimation techniques.

3 Shaker-beam Simulation Results

To demonstrate the proposed control methodology, we perform numerical simulations of the shaker-beam system shown in Figure 4a. The model of the structure is an Euler-Bernoulli cantilever beam [45], with a nonlinear spring attached at its free end. The shaker is modelled as an electromechanical system, where the mechanical subsystem, capturing the armature motion, is represented by a linear mass-spring-damper system. The electrical subsystem is in the form of an RL circuit, which includes the back-emf (electromotive force). A rigid connection between the shaker and the structure is also assumed. This assumption stems from the fact that the stinger is axially very stiff compared to the beam structure. This assumption is made in order to reduce the model complexity and is not crucial to the performance of the control algorithm.

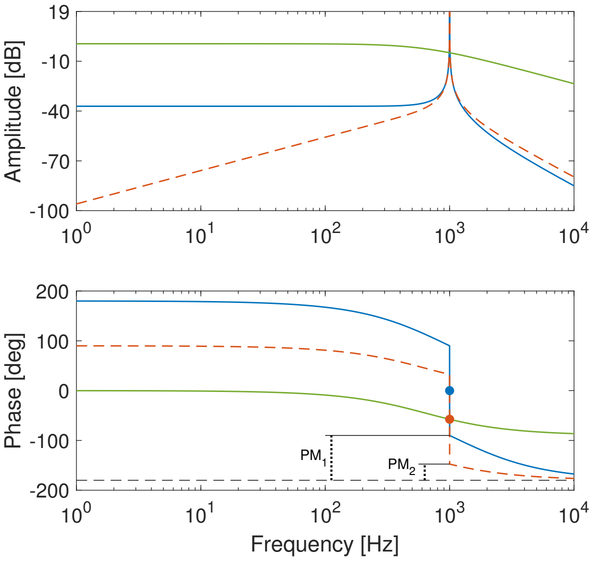

Fig. 3: Bode plot of the uncontrolled plant $P(j\omega)$ (——) and plant with the controller $C(j\omega)P(j\omega)$ (2.16) when $\phi = \phi_p$ (——) and $\phi = 0$ (- - -) for the reference/disturbance frequency of $1kHz$ (chosen to highlight the difference between different choices of ϕ); Average value of the discontinuous phase when $\phi = \phi_p$ (●) and $\phi = 0$ (●); PM_1 and PM_2 are the phase margins corresponding to $\phi = \phi_p$ and $\phi = 0$, respectively.

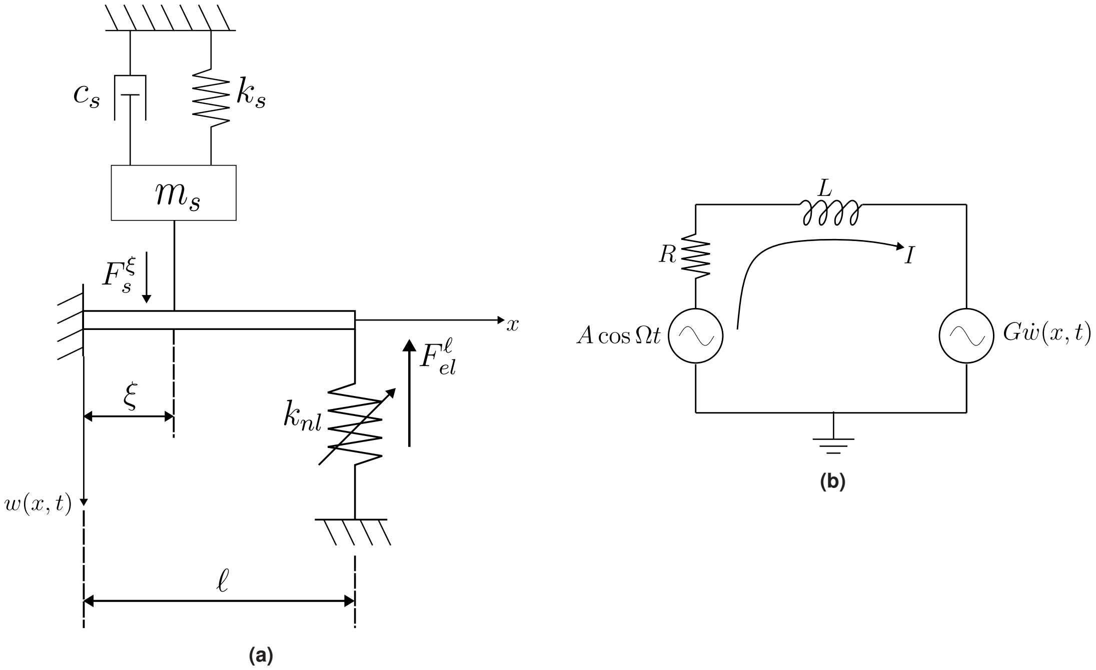

Fig. 4: (a) Shaker-beam model; (b) Electrical model of the shaker coil

Approximating the beam's motion using its first two (mass-normalized) modes, the equations of motion of the coupled

Parameter	**Value**	**Unit**	**Obtained from**
m_s	0.04	kg	Datasheet
c_s	1.5875	Ns/m	Pluck test [48]
k_s	$1.0198e+04$	N/m	Pluck test [48]
L	$2.5e-04$	H	Measured
R	1	Ω	Measured
G	12.3	N/A	Calculated: $G = V_{emf}/\dot{x}$ [1]
$f_1(\frac{\omega_1}{2\pi})$	14.6	Hz	Multisine excitation [49]
$f_2(\frac{\omega_2}{2\pi})$	48.8	Hz	Multisine excitation [49]
ζ_1	0.03	-	Half-power bandwidth [50]
ζ_2	0.09	-	Half-power bandwidth [50]
k_{nl}	$42.5e+05$	N/m^3	Static test
ℓ	$350e-03$	m	Measured
ξ_1	$60e-03$	m	Measured
ξ_2	$17.5e-03$	m	Simulation only
$\phi(L)$	$[-7.3821,\ 7.3608]$	$1/\sqrt{kg}$	Linear cantilever beam without shaker [45]
$\phi(\xi_1)$	$[-0.3281,\ -1.7140]$	$1/\sqrt{kg}$	Linear cantilever beam without shaker [45]
$\phi(\xi_2)$	$[-0.0294,\ -0.1846]$	$1/\sqrt{kg}$	Linear cantilever beam without shaker [45]
K	100	-	-
ϕ	-	rad/s	From shaker coil FRF [2]

Table 1: Shaker-beam simulation parameters

beam-shaker structure are given by:

$$\begin{aligned}
&\begin{bmatrix} 1+m_s\phi_1^2(\xi) & m_s\phi_1(\xi)\phi_2(\xi) \\ m_s\phi_1(\xi)\phi_2(\xi) & 1+m_s\phi_2^2(\xi) \end{bmatrix}\ddot{\boldsymbol{\eta}} + \begin{bmatrix} 2\zeta_1\omega_1 + c_s\phi_1^2(\xi) & c_s\phi_1(\xi)\phi_2(\xi) \\ c_s\phi_1(\xi)\phi_2(\xi) & 2\zeta_2\omega_2 + c_s\phi_2^2(\xi) \end{bmatrix}\dot{\boldsymbol{\eta}} \\
&+ \begin{bmatrix} \omega_1^2 + k_s\phi_1^2(\xi) & k_s\phi_1(\xi)\phi_2(\xi) \\ k_s\phi_1(\xi)\phi_2(\xi) & \omega_2^2 + k_s\phi_2^2(\xi) \end{bmatrix}\boldsymbol{\eta} + \begin{bmatrix} \phi_1(\ell) \\ \phi_2(\ell) \end{bmatrix} k_{nl}\left(\begin{bmatrix} \phi_1(\ell) & \phi_2(\ell) \end{bmatrix}\boldsymbol{\eta}\right)^3 \qquad (3.1) \\
&= G\begin{bmatrix} \phi_1(\xi) \\ \phi_2(\xi) \end{bmatrix} I,
\end{aligned}$$

$$L\dot{I} + RI + G\begin{bmatrix} \phi_1(\xi) & \phi_2(\xi) \end{bmatrix}\dot{\boldsymbol{\eta}} = A\cos\Omega t, \qquad (3.2)$$

where $\boldsymbol{\eta} = [\eta_1\ \eta_2]^T$ are the modal coordinates for the first and second modes, respectively. $\phi_i(\ell)$ and $\phi_i(\xi)$ correspond to the mode shape i at points ℓ and ξ along the beam. The measured force is given by $F = GI$. The parameters used for the simulation are given in Table 1, where K refers to the controller gain. The parameters roughly correspond to the experimental setup in section 4.1, but it should be noted that no particular care was taken to accurately identify them, as they are not used for the controller design. The mode shapes at points ℓ and ξ are calculated for the case of a linear cantilever beam in order to obtain a closed-form solution.

More detailed multiple-degree-of-freedom shaker models could have been used (e.g. [46, 3, 47]), but they are not considered in this work because our objective is to develop an exciter force control algorithm that does not rely on a detailed knowledge of the exciter system. As such, no attempts have been made to precisely match the shaker model structure or even calibrate its parameters against the shaker used during the tests presented in Section 4.

Simulations of the shaker-beam model (3.1)–(3.2) are first performed with a sinusoidal input voltage at $21Hz$. Figure 5a(green) shows that this mono-harmonic voltage results in a multi-harmonic excitation force (Figure 5b(green)) due to the presence of nonlinearity. Figure 5b(blue) shows that applying the AFC controller can eliminate the harmonic distortions present in the force by adding them to the input voltage (5a(blue)). Similar results are observed for other excitation frequencies but are not presented here for conciseness. A wider range of frequencies will be shown in the experimental section.

Although the controller is designed based on steady-state assumptions, it can potentially be used to reject slowly changing disturbances such as those arising from sine sweep excitations. This is illustrated in Figure 6 where the excitation force obtained without (green) and with (blue) force control are compared to a single-tone $10N$ reference force (orange) when the shaker is attached at 17% (Figure 6a) and 5% (Figure 6b) of the beam's length. The sweep rate is $10rad/s^2$. When the controller is not active (green), the force exhibits not only harmonic distortions but also exhibits the well-known force drop out near the resonance (particularly noticeable in Figure 6a). In contrast, repeating the sweep with the controller active (blue) yields a different shaker response that matches the force reference (orange)

---

[1] The velocity is obtained by differentiating the displacement measurement from a pluck test, and the back-electromotive force is measured at the shaker terminals, while the amplifier is disconnected.

[2] Shaker coil is considered as $L\dot{I} + RI = u$. The phase parameter depends on the excitation frequency, and the values can change significantly, which is why they are omitted from the table. It should be noted that the model is a considerable simplification of the real testing conditions, and $\phi = 0$ would also work in this case.

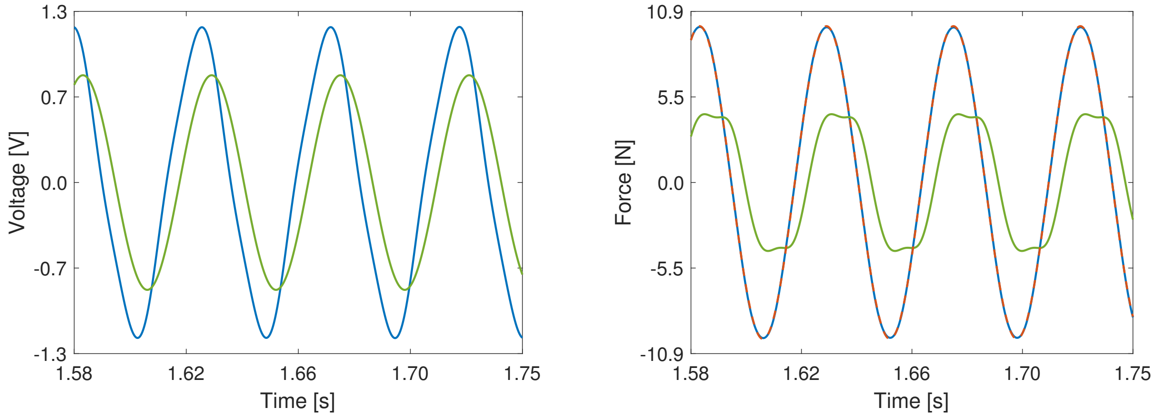

(a) **(b)**

Fig. 5: (a) Shaker input voltage with (——) and without (——) control in steady-state motion; (b) Shaker force with (——) and without (——) without control under steady-state motion, (- - -) Reference force for the controller; Excitation is at the frequency of $21Hz$

over a wider frequency range. However, a force overshoot can be observed just before $35Hz$ in Figure 6a. This overshoot occurs when a saddle-node bifurcation is encountered near the resonance, leading to the well-known jump-down phenomenon and fast transients that cannot be dealt with by the controller.

When the shaker is connected closer to the fixed end (Figure 6b), both the force drop-out and the higher harmonics distortions are reduced considerably, even without control. The reason for the reduction in the disturbances is that the amplitude of the beam's motion (and hence velocity) is significantly smaller closer to the fixed end, resulting in much smaller interactions with the electrical shaker dynamics. While the appropriate positioning of the shaker seemingly removes the force disturbance, this approach cannot generally be used in practice because it limits the vibration levels that can be achieved during the experiment, potentially affecting subsequent nonlinear dynamic characterisation and system identification.

The effect of the force control on the structure response is shown in Figure 7, where green and blue are the responses obtained without and with force control, respectively; and the orange curve corresponds to a reference frequency response curve (FRC) obtained at a constant forcing amplitude using numerical continuation [51], using COCO continuation package for MATLAB [52]. Figure 7a shows that, without force control, the response of the structure is significantly different from the response with force control and the reference FRC. A slow drift from the reference FRC is first noticeable before the response jumps down prematurely compared to the reference FRC. This is primarily due to the force drop that significantly reduces the vibration levels achieved near resonance. This could lead to improper characterization of the structure's nonlinear resonance amplitude and frequency if not accounted for. In contrast, when the force controller is active, the response of the shaker-beam system matches the reference FRC computed using continuation. Numerical continuation is capable of showing the unstable periodic responses of the structure (dashed orange lines), which is not possible using a forward frequency sweep and without additional control of the structure response [28, 29, 22, 6].

4 Shaker-beam Experimental Results

4.1 Experimental Shaker-beam Setup

The proposed control method is now demonstrated on the experimental setup shown in Figure 8. It consists of a thin, flexible cantilever beam made of steel, with two springs at its free end. The springs are linear, but they deform in a direction orthogonal to their natural direction of elongation, introducing (geometric) nonlinearity. The structure exhibits a 3:1 mode interaction between its first two bending modes if the beam length and spring pre-tension are appropriately adjusted [14]. The physical dimensions of the beam are $350x30x2mm$, and the shaker is attached $60mm$ away from the fixed end (i.e. $\approx 17\%$ of the beam's length).

A DataPhysics V4 shaker, powered by DataPhysics PA30E amplifier, is used to excite the structure. To measure the displacement of the beam at its tip, an Omron ZX2-LDA laser displacement sensor is used. The force and acceleration of the shaker are measured by a PCB Piezotronics 288D01 impedance head. The acceleration measurement is not

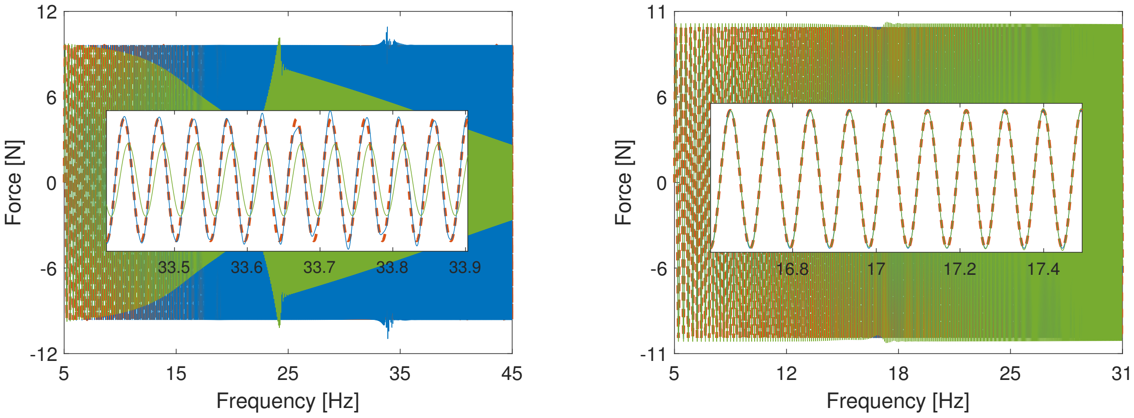

(a) **(b)**

Fig. 6: (——) Reference force; (a) Shaker force (——) with and (——) without control during a sine sweep when shaker is attached at 17% of beam length; (b) Shaker force (——) with and (——) without control during a sine sweep when shaker is attached at 5% of beam length

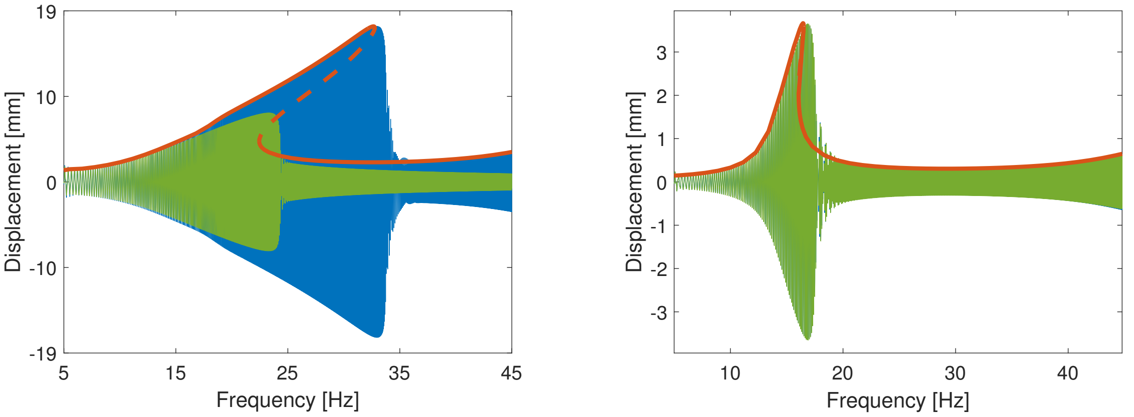

(a) **(b)**

Fig. 7: (——) Beam displacement when the controller is active with a 10N reference force; (——) Beam displacement when the controller is not active; (——) Beam reference response from numerical continuation (stable branch); (- - -) Beam reference response from the numerical continuation (unstable branch); (a) Shaker attached at 17% of the beam length; (b) Shaker attached at 5% of the beam length

used in the rest of this work. A dSPACE MicroLabBox was used as the platform for data acquisition and real-time control.

The plant to control, $P(j\omega)$, is considered as the transfer function between the input voltage and the force measured by the impedance head. The plant phase, ϕ, which is used in the controller, was obtained from the FRF identified using broadband multisine excitation, i.e. a sum of sinusoidal signals in the frequency range of interest, where the phase of each component is chosen randomly from $[0,\ 2\pi[$ interval [49]. The level of multisine excitation was kept low, but no particular care was taken to adjust the amplitude, or even to obtain a 'best linear approximation'. The identified phase parameter was subsequently implemented in the MicroLabBox as a lookup table. Five harmonics are controlled in parallel, and the controller gains K were all set to 1, as this was found to be small enough to separate the timescale of the coefficient adaptation from the timescale of the vibration of the structure. It should be noted that the FRF estimation procedure should be repeated once the shaker is connected to a new structure, as the applied force depends on the properties of the structure as well.

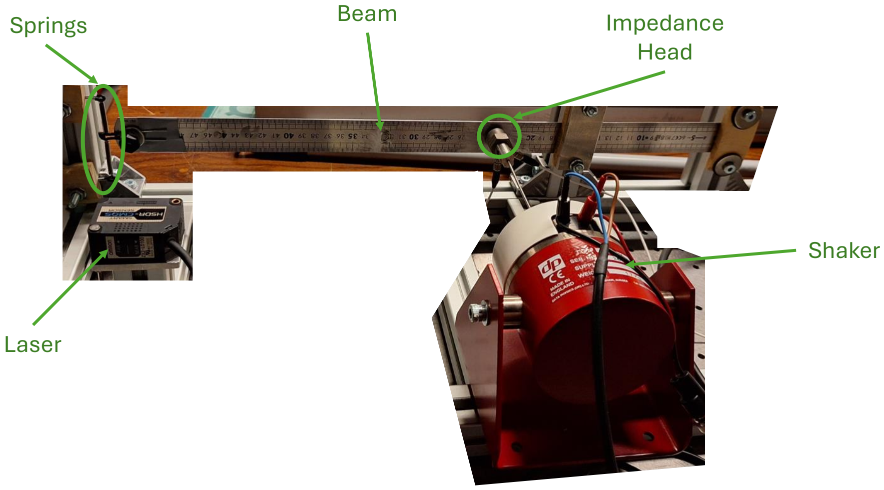

Fig. 8: Shaker-beam experimental rig

4.2 Open-Loop Stepped Sine Testing

Initial open-loop tests reveal the complex dynamic behaviour of the nonlinear structure. Figure 9a shows the response curves obtained for increasing input voltage amplitudes. A clear hardening behaviour, including the appearance of coexisting responses, is observed. As expected, a sudden jump in vibration amplitude occurs as the resonance is approached. This transition is represented by a black dashed line in Figure 9a. The strong influence of the higher harmonics can be observed in the displacement of the structure as the vibration amplitude increases (see the colour scheme in Figure 9a, which represents the total harmonic distortion (THD) relative to the amplitude of the fundamental harmonic). THD definition considered here is given by $\mathrm{THD} = \sqrt{\sum_{i=2}^{N} A_i^{rms}}/A_1^{rms}$ where A_i^{rms} is the root mean square amplitude of the ith harmonic component [53] and $N = 7$.

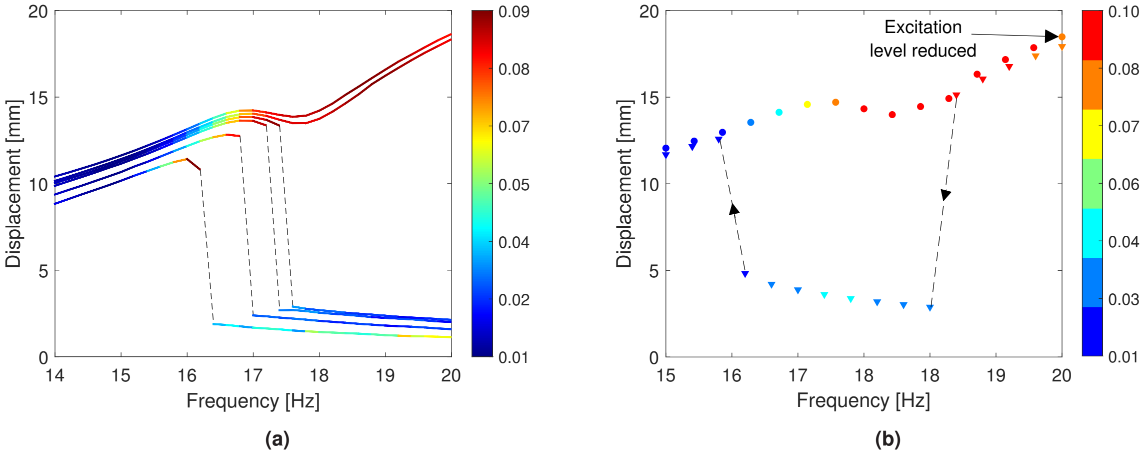

Fig. 9: (a) Frequency response of the beam without force control, for input voltage levels of: $1.2V, 1.8V, 2.4V, 2.6V, 2.8V, 3V$; (b) Upwards stepped sine, followed by a downwards stepped sine at a lower excitation level; Colour scheme represents total harmonic distortion relative to the fundamental amplitude

Figure 9 also indicates the presence of isolated responses, which for this system are due to the presence of a modal interaction [54, 55, 56, 14]. For the highest two excitation levels in Figure 9a, the isolated response curve has merged with the main branch of the frequency response. Prior to this merging, the frequency response is seen to saturate, i.e. fixed excitation level increments result in increasingly smaller changes near the resonance until the isola merges with the main response branch [56]. Note that, after the jump-down near resonance, we observe a higher THD in the response curve corresponding to the lowest voltage amplitude. This increase appears to result from high-frequency

components present in the signal, the origin of which remains unclear.
To observe responses on the isolated curve, a stepped sine excitation is performed from $14Hz$ to $20Hz$, taking steps of $0.2Hz$ (bullet markers in Figure 9b). At $20Hz$, the structure response lies on a section of the resonance peak that corresponds to the isola for lower excitation levels. The excitation level is then decreased and the frequency is stepped downwards from $20Hz$ back to $14Hz$ (triangle markers in Figure 9b). For this second stepped sine test, an isolated region of high-amplitude responses can be observed between $20Hz$ and $18.5Hz$. A more systematic way of observing these types of responses can be achieved using control-based continuation, as in [28].

The voltage, force and response frequency contents for the responses shown in Figure 9 (at the voltage level of $2.6V$) are presented in Figure 10(a, b, c). The amplitude (represented by the colour scheme) is normalized by the amplitude of the fundamental component at 14 Hz. For a sinusoidal input voltage, the force distortions (fundamental amplitude and higher harmonics) resulting from the exciter-structure interaction are clearly visible. In particular, a 3rd and 5th harmonic appear as the vibration amplitude increases. The force drop-out phenomenon is also visible.

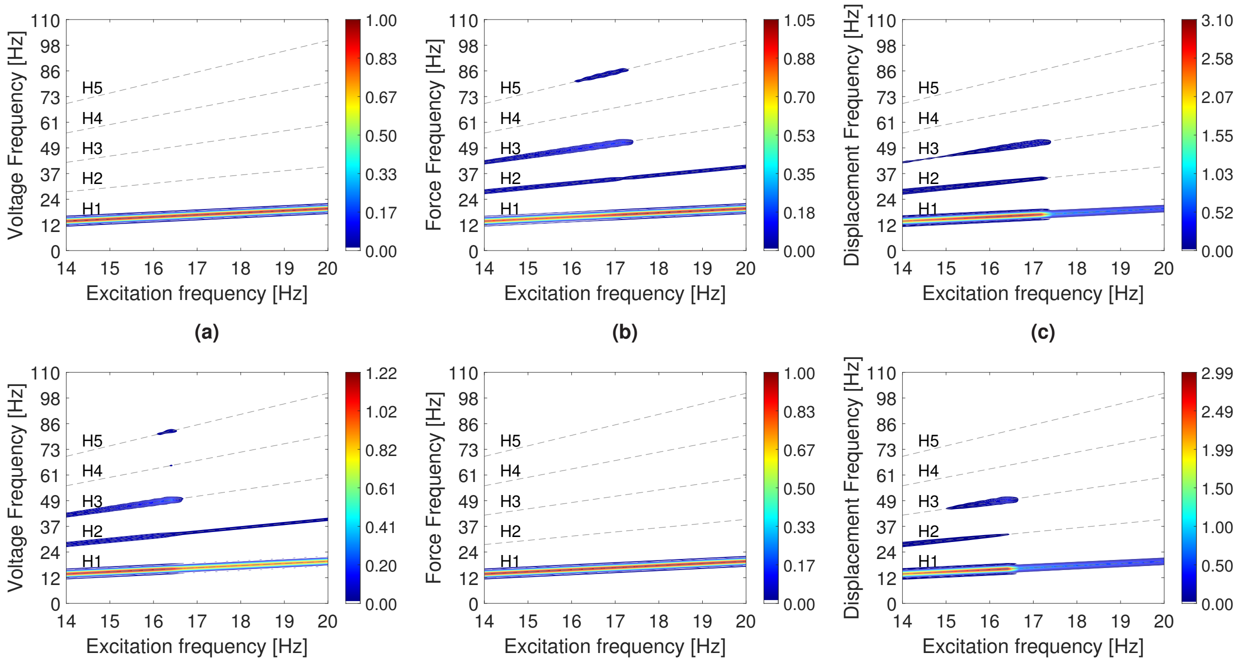

(a) **(b)** **(c)**

(d) **(e)** **(f)**

Fig. 10: Plot of excitation frequency vs frequency content of the measurement signal during a stepped sine test on the main response branch; Colour represents amplitude of the measurement signal normalized with respect to the starting amplitude of the fundamental harmonic of the signal; Dashed lines signify the frequency of the first five harmonics during the stepped sine test; (a) Shaker input voltage without control; (b) Shaker force without control; (c) Beam tip displacement without control; (d) Shaker input voltage with control; (e) Shaker force with control; (f) Beam tip displacement with control

4.3 Force-controlled Stepped Sine Testing

The capability of the proposed AFC control methodology to maintain a monoharmonic force of $11N$ is now demonstrated. This force level corresponds approximately to the force amplitude obtained with a $2.6V$ input voltage at $14Hz$, and without control. Figures 10(d) and 10(e) show that the frequency content of the applied force is now monoharmonic thanks to the introduction of higher harmonics in the voltage. The fundamental voltage amplitude also changes with the excitation frequency to overcome the force dropout phenomenon and achieve a constant force amplitude. Figure 10(f) also shows the effect of the change in force profile on the frequency content of the beam response. The total harmonic distortion in the force achieved with AFC is below 0.025% for all but one of the periodic responses shown in Figure 10(e), compared to up to 20% before control. 1% total harmonic distortion is achieved for the point where the jump has occurred. This larger error is thought to be the result of longer transients and the controller not completely settling. Similar performances are obtained for lower force levels (not shown for conciseness).

When the excitation level is sufficiently high (just beyond $11N$), the isola merges with the main branch (as observed in Figure 9) and quasi-periodic responses are observed around the merging point. This type of disturbance is not easily parametrized by a Fourier series as in the case of integer harmonics. As such, the controller is, at best, ineffective at rejecting this type of disturbance (see Figure 11). The same could be said in the case of chaotic responses, where a much richer frequency spectra can be observed [57].

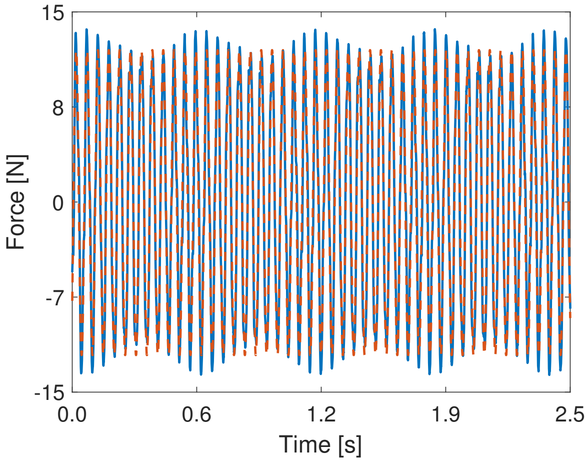

Fig. 11: Force reference tracking during a quasi-periodic response; (- - -) Reference force; (——) Measured force.

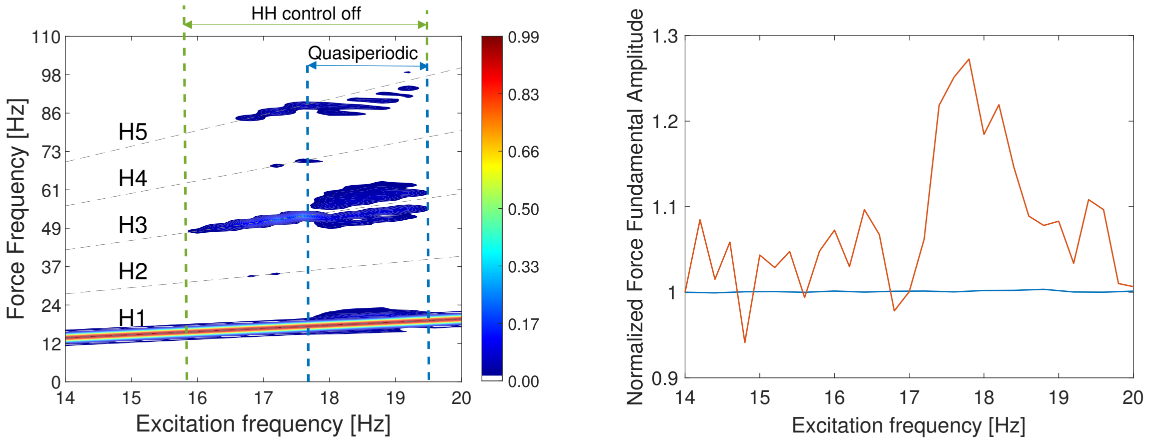

(a) **(b)**

Fig. 12: (a) Plot of excitation frequency vs frequency content of the measurement signal during a stepped sine test on the merged response branch; Colour represents amplitude of the measurement signal normalized with respect to the starting amplitude of the fundamental harmonic of the signal; (b) Relative variation of the fundamental force component over the frequency range of the stepped sine test with (——) and without (——) control; The values are normalized with respect to the fundamental component at $14Hz$

In practice, we observed that controllers acting on the higher harmonics could sometimes lead to instability and had to be turned off even before the quasi-periodic region (see Figure 12a). The reason is that the phase of the 3rd harmonic had changed significantly due to the interaction between the first and second bending modes. The phase parameter ϕ associated with the 3rd harmonic was therefore significantly different from the value estimated at low vibration amplitudes, which impacted the stability of the closed-loop system. Developing an online estimation of the exciter's phase could address the problem, but this is outside the scope of this paper. Figure 12b shows the good performance of the fundamental harmonic force control achieved in this region, with amplitude errors on the fundamental force amplitude lower than 0.34%. In contrast, large variations are observed during the open-loop test.

4.4 Step Response of the Controller

In this section, we discuss the transient performance of the controller when the amplitude or frequency of the reference force is changed. Figure 13a shows the controller response during a large step in the reference amplitude (from $5N$ to $12N$). It is seen that the controller converges relatively quickly ($\approx$ 5 oscillation cycles) to the new reference. Similar observations can be made for a step change in the oscillation frequency (from $7Hz$ to $14Hz$), as shown in Figure 13b.

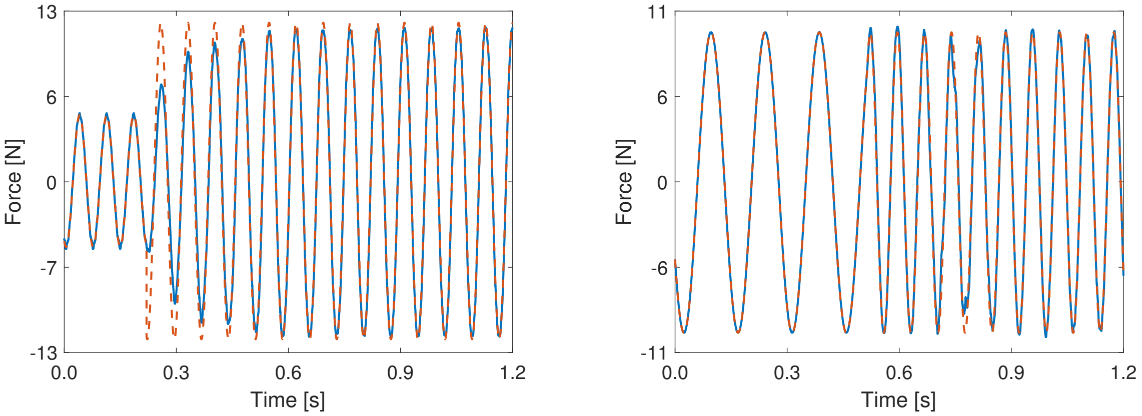

(a) **(b)**

Fig. 13: (- - -) Reference force; (——) Measured force; (a) Force reference tracking during a step change of the reference amplitude from 5N to 12N; (b) Force reference tracking during a step change of the reference frequency from 7Hz to 14Hz

The tracking of multi-harmonic references can also be achieved with AFC. Figure 14a illustrates that a step change from a single-harmonic to two-harmonic reference signals can be achieved relatively quickly ($\approx$ 4 oscillation cycles). Figure 14b further demonstrates that achieving a new reference signal with multiple higher harmonics does not present any particular challenges. The ability to track multi-harmonic reference signals shows that AFC could, in principle, be successfully exploited for the purpose of nonlinear force appropriation [58], where multi-harmonic excitations are a priori necessary to accurately isolate the nonlinear normal modes of the structure.

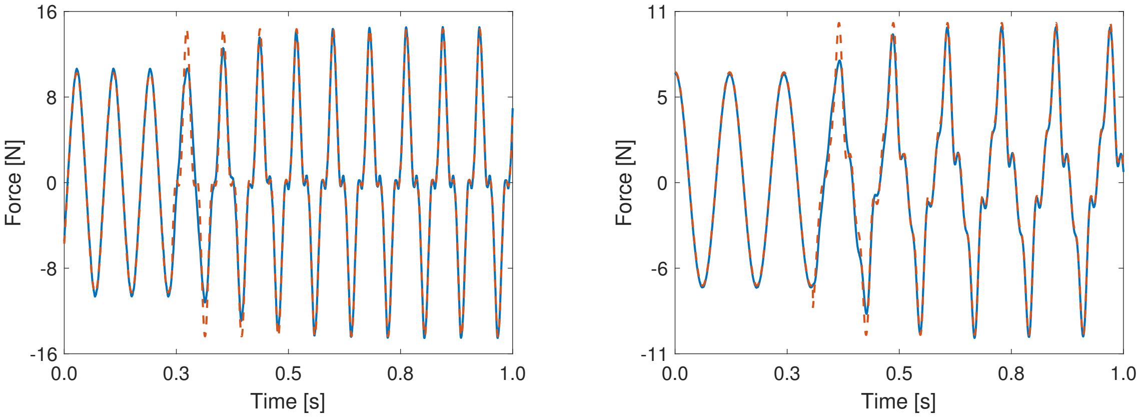

(a) **(b)**

Fig. 14: (- - -) Reference force; (——) Measured force; (a) Force reference tracking during a step change of the reference amplitude from 10N fundamental to $10N$ fundamental+$4N$ 3rd harmonic; (b) Force reference tracking for the reference amplitude of $7N$ fundamental+$2N$ 3rd harmonic+$2N$ 5th harmonic

4.5 Force-controlled Sine Sweep Testing

As illustrated numerically in Section 3, the proposed control methodology can also be applied during a sine sweep excitation, although with potentially degraded performance. Figure 15a shows that, after an initial transient, a good reference tracking is achieved for an excitation amplitude of $10N$ and a relatively fast sweep rate of $1\ Hz/s$. As the jump frequency is approached, a more significant error is observed (see Figure 15c). Improved force control performances are achieved with a slower sweep rate of $0.2\ Hz/s$, as shown in Figures 15b and 15d. However, the tracking error is not completely eliminated, which again highlights the fact that the AFC controller was designed for steady-state operation.

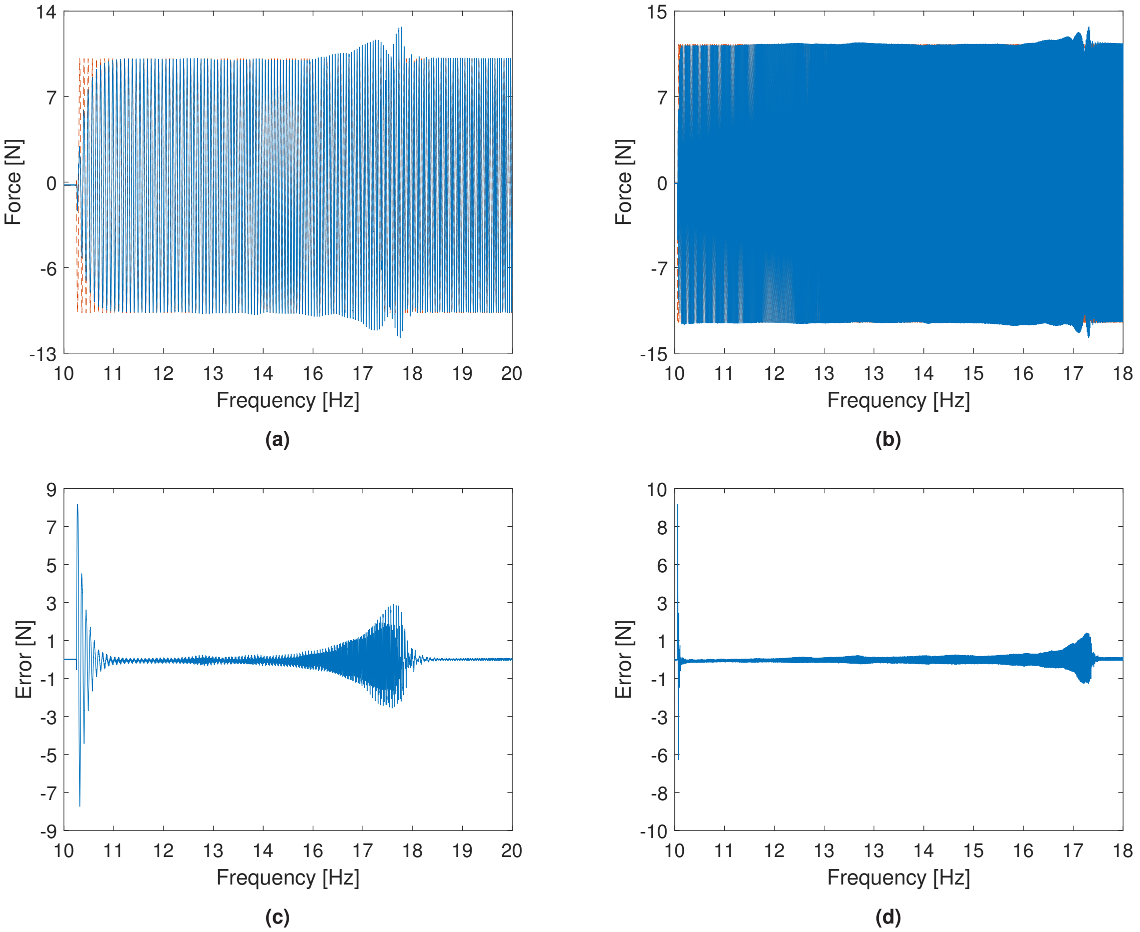

(a) **(b)** **(c)** **(d)**

Fig. 15: (a) Force reference tracking during a sine sweep from $10Hz$ to $20Hz$, with the sweep rate of $1Hz/s$; (——) Reference force; (——) Measured force; (b) Force reference tracking during a sine sweep from $10Hz$ to $17.6Hz$, with the sweep rate of $0.2Hz/s$; (c) Tracking error during a sine sweep from $10Hz$ to $20Hz$, with the sweep rate of $1Hz/s$; (d) Tracking error during a sine sweep from $10Hz$ to $17.6Hz$, with the sweep rate of $0.2Hz/s$

4.6 Sensitivity to Control Parameters

Figure 16 illustrates the importance of the phase parameter by comparing the performance of the controller with and without it. The force parameters considered are: fundamental amplitude $7N$, frequency $15Hz$, and phase lead parameters $7.8°, -41.06°, -72.8°, -60.77°, -116.91°$ for the first five harmonics. In this particular example, setting the phase parameter to 0 results in an unstable behavior of the closed-loop system.

5 Shaker-blade Experimental Results

Aero-engine components, and specifically blades and vanes that are in the gas path, get subjected to significant and often sustained dynamic loads. It is therefore paramount to assess their structural integrity which is often done in the form of High Cycle Fatigue testing. With the optimised design and much better engineering materials, the HCF strength of these components, and, subsequently the levels at which they need to be excited are getting higher. The

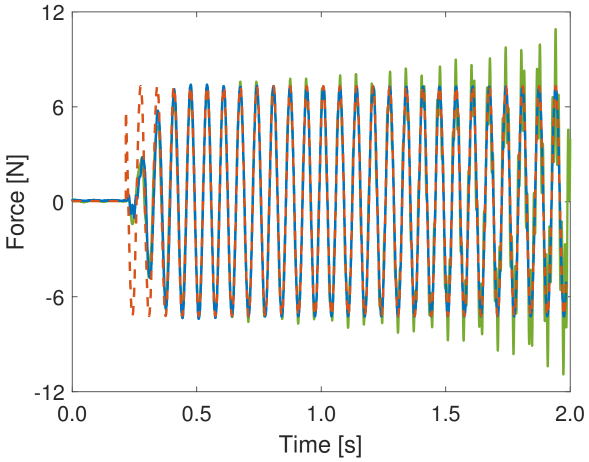

Fig. 16: (- - -) Reference force; (——) Measured force with the phase lead parameter; (——) Measured force without the phase lead parameter; Force reference tracking with and without phase lead parameter

result of all of this is that the components get driven to a nonlinear regime, which, when combined with exciter-structure interactions, results in a complex, uncontrolled harmonic spectrum of the force. Such harmonic distortions are now illustrated on an industrial component – a compressor blade from Rolls-Royce's aero-engine (see Figure 17), and the proposed controller method is applied to recover an ideal sinusoidal forcing without distortions.

The blade is clamped in a support frame, whose main purpose is to load the blade root without introducing significant parasitic damping. A DataPhysics V20 shaker is used to excite the structure, along with a DataPhysics PA100E amplifier. The displacement of the blade is measured close to its tip by an Omron ZX2-LDA laser displacement sensor. The force and acceleration of the shaker are measured by a PCB Piezotronics 288D01 impedance head.

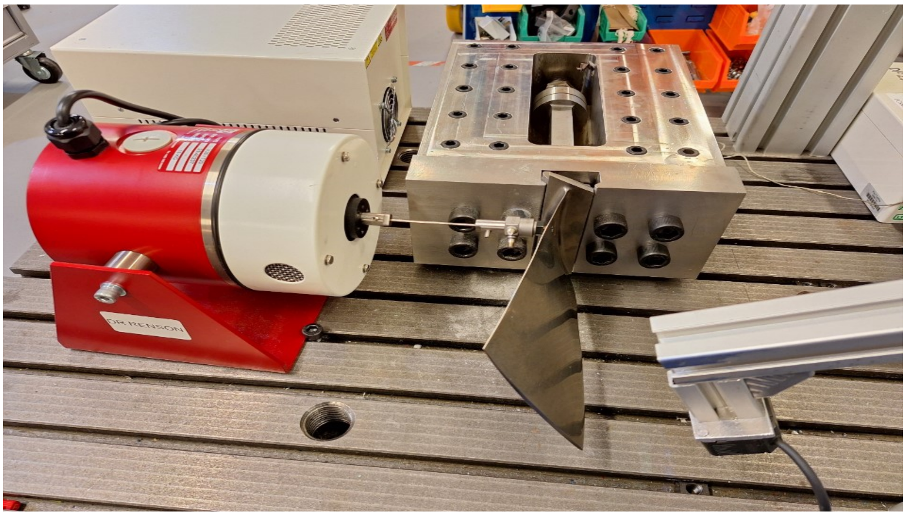

Fig. 17: Shaker-blade experimental rig

Initial open-loop sine sweeps show that the structure exhibits a softening behavior (Figure 18a). Figure 18b shows the force measured during the sine sweeps obtained at the increasing voltage levels (normalized by the highest level). 3rd harmonic distortions are clearly visible for the three highest excitation levels (yellow, orange and blue). Note also an almost 180° flip in the phase of the yellow force signal compared to other force levels (see close-up in Figure 18b). As discussed in Section 4.3, such changes in phase of the fundamental or higher harmonics can lead to poor performance or even instabilities and would require a real-time estimation of the phase parameter instead of its a priori identification.

Figure 19 shows the results obtained for an open-loop and force-controlled stepped sine test. To have comparable excitation levels between the two tests, the target force amplitude used during control tests corresponds to the force

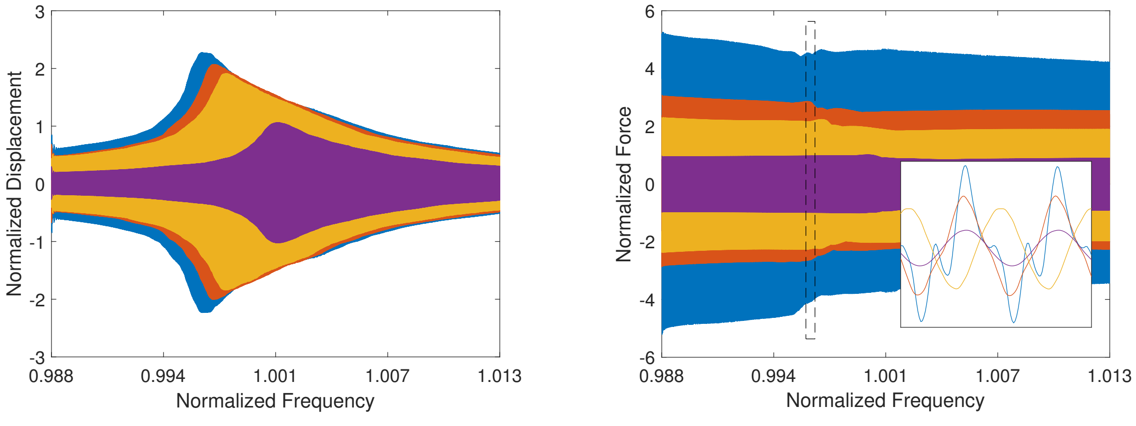

(a) **(b)**

Fig. 18: Open-loop sine sweeps for normalized input voltage levels of: $0.27, 0.64, 0.82, 1$; Axes are normalized in order to hide true values; (a) Displacement; (b) Force

achieved at a normalised excitation frequency of 0.988 in the open-loop test. Some harmonic distortions (2nd and 3rd harmonics) are noticeable in open-loop (Figure 19)(a), and they are successfully rejected by AFC (Figure 19)(b). The total harmonic distortions without and with force control are 3.14% and 0.54%, respectively, demonstrating the performance of the proposed methodology. Unfortunately, higher force levels could not be achieved experimentally as the connection between the shaker and the locally-curved blade surface would systematically break.

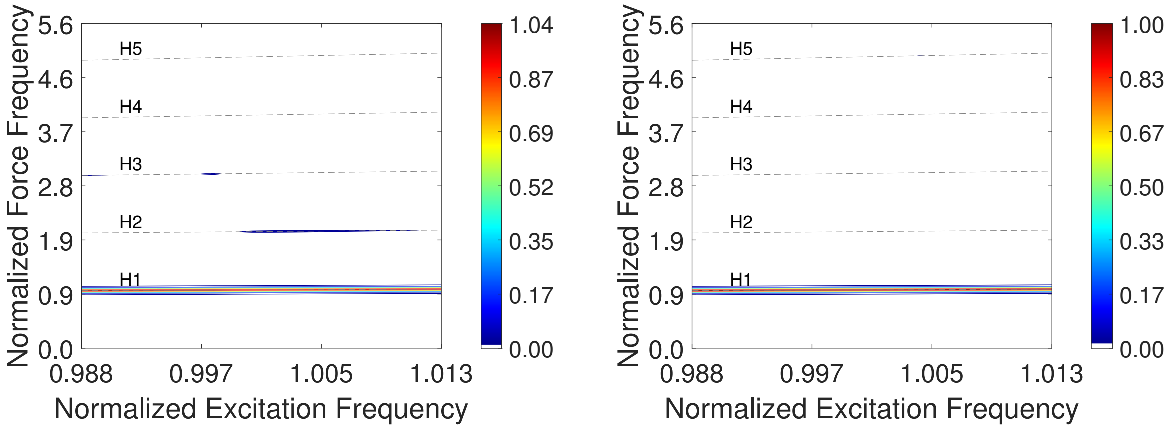

(a) **(b)**

Fig. 19: Plot of excitation frequency vs frequency content of the measurement signal during a stepped sine test; Colour represents amplitude of the measurement signal normalized with respect to the starting amplitude of the fundamental harmonic of the signal; (a) Open-loop force; (b) Closed-loop force

6 Conclusion and Future Work

In this paper, exciter force control was formulated as a disturbance rejection problem, where the unknown disturbance is the result of the coupling between the exciter and a nonlinear structure. The framework behind the AFC technique was then successfully exploited in order to reject the higher harmonics originating from the nonlinear structure, while also preventing the force drop-out phenomenon. This is achieved without assuming any knowledge about the structure and utilizing only the phase of the exciter. The tuning of the controller was not found to be challenging. Addition of the phase parameter was found to greatly improve stability and transient response, making the controller more robust. This, in turn, means that suboptimal controller gains have a smaller impact on the performance. Although, it was found during the experiments that the gains should be kept small enough in order to preserve stability, which is in accordance with the averaging analysis of adaptive systems. This allows a straightforward application of the controller in an experimental setting. The limitation of the current force control method is that it cannot eliminate non-periodic disturbances such as those arising from quasi-periodic oscillations. Including real-time estimation of the phase would also be beneficial, as it would simplify the testing of the structures exhibiting modal interactions. This will be investigated in the future.

The force control methodology could further be exploited within the framework of CBC and PLL testing methods, in order to produce more accurate backbone and frequency response curves. Additionally, it could serve as an important building block for nonlinear force appropriation techniques.

Acknowledgements

The authors would like to thank Rolls-Royce Plc. for providing the financial support for this project (iCASE #230134) and for giving permission to publish this work. The authors also acknowledge the financial support of the EPSRC (grant #EP/Y528560/1).

Supplementary material

The data from the shaker-beam experiment is available at [60], along with the post-processing scripts to generate the figures from section 4.

Appendix

A Averaging Analysis

The time domain steady-state response of the linear plant P(s) to harmonic excitation can be expressed as:

$$P(s)\,[\boldsymbol{\varphi}] = \begin{bmatrix} P(s)[\cos(\omega t)] \\ P(s)[\sin(\omega t)] \end{bmatrix} = \begin{bmatrix} P(s)[\frac{e^{j\omega t}+e^{-j\omega t}}{2}] \\ P(s)[\frac{e^{j\omega t}-e^{-j\omega t}}{2j}] \end{bmatrix} = \frac{1}{2}\begin{bmatrix} P(s)[(e^{j\omega t}+e^{-j\omega t})] \\ -jP(s)[(e^{j\omega t}-e^{-j\omega t})] \end{bmatrix}, \tag{A1}$$

where $P(s)[\cdot] : \mathcal{F} \to \mathcal{F}$ is regarded as an operator which takes in a time domain function as the input and produces a 'filtered' time domain function as the output and $\mathcal{F} : \mathbb{C} \to \mathbb{C}$. This notation of mixed time and frequency domain values is commonly used in adaptive control in order to avoid complicated expressions [59].
Considering that an input with frequency $\pm\omega$ will produce an output only at that frequency, substituting $P(s)|_{s=\pm j\omega}$ in (A1) gives:

$$\begin{aligned} P(s)\,[\boldsymbol{\varphi}]|_{s=\pm j\omega} &= \frac{1}{2}\begin{bmatrix} P(j\omega)e^{j\omega t} + P(-j\omega)e^{-j\omega t} \\ -jP(j\omega)e^{j\omega t} + jP(-j\omega)e^{-j\omega t} \end{bmatrix} \\ &= \frac{1}{2}\begin{bmatrix} P(j\omega)e^{j\omega t} + P^{*}(j\omega)e^{-j\omega t} \\ -jP(j\omega)e^{j\omega t} + jP^{*}(j\omega)e^{-j\omega t} \end{bmatrix} \\ &= \frac{1}{2}\begin{bmatrix} H_1 \\ H_2 \end{bmatrix}, \\ H_1 = {} & (Re\{P(j\omega)\} + jIm\{P(j\omega)\})(\cos\omega t + j\sin\omega t) \\ & + (Re\{P(j\omega)\} - jIm\{P(j\omega)\})(\cos\omega t - j\sin\omega t) \\ = {} & 2Re\{P(j\omega)\}\cos\omega t - 2Im\{P(j\omega)\}\sin\omega t, \\ H_2 = {} & -j(Re\{P(j\omega)\} + jIm\{P(j\omega)\})(\cos\omega t + j\sin\omega t) \\ & + j(Re\{P(j\omega)\} - jIm\{P(j\omega)\})(\cos\omega t - j\sin\omega t) \\ = {} & 2Re\{P(j\omega)\}\sin\omega t + 2Im\{P(j\omega)\}\cos\omega t, \end{aligned} \tag{A2}$$

where $P^{*}(j\omega)$ is the complex-conjugate of $P(j\omega)$.
Finally, (A2) is expressed as:

$$P(s)\,[\boldsymbol{\varphi}] = \begin{bmatrix} H_1' \\ H_2' \end{bmatrix} = \begin{bmatrix} Re\{P(j\omega)\}\cos\omega t - Im\{P(j\omega)\}\sin\omega t \\ Re\{P(j\omega)\}\sin\omega t + Im\{P(j\omega)\}\cos\omega t \end{bmatrix}. \tag{A3}$$

Using (A3), the average of $\mathbf{z} = \boldsymbol{\varphi}' P(j\omega) \left[\boldsymbol{\varphi}^T\right]$ can now be derived as:

$$\bar{\mathbf{z}} = \begin{bmatrix} \cos(\omega t + \phi) \\ \sin(\omega t + \phi) \end{bmatrix} \begin{bmatrix} H_1' & H_2' \end{bmatrix} = \begin{bmatrix} h_{11}' & h_{12}' \\ h_{21}' & h_{22}' \end{bmatrix}, \tag{A4}$$

where

$$\begin{aligned}
\bar{h}_{11}' &= \lim_{T\to\infty} \frac{1}{T} \int_0^T \left(Re\{P(j\omega)\} \cos\omega t \cos(\omega t + \phi) - Im\{P(j\omega)\} \sin\omega t \cos(\omega t + \phi)\right) dt \\
&= \lim_{T\to\infty} \frac{1}{T} \int_0^T \left(Re\{P(j\omega)\} \cos\omega t (\cos\omega t \cos\phi - \sin\omega t \sin\phi)\right. \\
&\quad \left. - Im\{P(j\omega)\} \sin\omega t (\cos\omega t \cos\phi - \sin\omega t \sin\phi)\right) dt \\
&= \frac{1}{2} \left(Re\{P(j\omega)\} \cos\phi + Im\{P(j\omega)\} \sin\phi\right), \\
\bar{h}_{12}' &= \lim_{T\to\infty} \frac{1}{T} \int_0^T \left(Re\{P(j\omega)\} \sin\omega t \cos(\omega t + \phi) + Im\{P(j\omega)\} \cos\omega t \cos(\omega t + \phi)\right) dt \\
&= \lim_{T\to\infty} \frac{1}{T} \int_0^T \left(Re\{P(j\omega)\} \sin\omega t (\cos\omega t \cos\phi - \sin\omega t \sin\phi)\right. \\
&\quad \left. + Im\{P(j\omega)\} \cos\omega t (\cos\omega t \cos\phi - \sin\omega t \sin\phi)\right) dt \\
&= \frac{1}{2} \left(-Re\{P(j\omega)\} \sin\phi + Im\{P(j\omega) \cos\phi\right), \\
\bar{h}_{21}' &= \lim_{T\to\infty} \frac{1}{T} \int_0^T \left(Re\{P(j\omega)\} \cos\omega t \sin(\omega t + \phi) - Im\{P(j\omega)\} \sin\omega t \sin(\omega t + \phi)\right) dt \\
&= \lim_{T\to\infty} \frac{1}{T} \int_0^T \left(Re\{P(j\omega)\} \cos\omega t (\cos\omega t \sin\phi + \sin\omega t \cos\phi)\right. \\
&\quad \left. - Im\{P(j\omega)\} \sin\omega t (\cos\omega t \sin\phi + \sin\omega t \cos\phi)\right) dt \\
&= \frac{1}{2} \left(Re\{P(j\omega)\} \sin\phi - Im\{P(j\omega)\} \cos\phi\right), \\
\bar{h}_{22}' &= \lim_{T\to\infty} \frac{1}{T} \int_0^T \left(Re\{P(j\omega)\} \sin\omega t \sin(\omega t + \phi) + Im\{P(j\omega)\} \cos\omega t \sin(\omega t + \phi)\right) dt \\
&= \lim_{T\to\infty} \frac{1}{T} \int_0^T \left(Re\{P(j\omega)\} \sin\omega t (\cos\omega t \sin\phi + \sin\omega t \cos\phi)\right. \\
&\quad \left. + Im\{P(j\omega)\} \cos\omega t (\cos\omega t \sin\phi + \sin\omega t \cos\phi)\right) dt \\
&= \frac{1}{2} \left(Re\{P(j\omega)\} \cos\phi + Im\{P(j\omega)\} \sin\phi\right),
\end{aligned}$$

where the only non-zero terms are the ones resulting from multiplication of $\cos\omega t$ (or equivalently $\sin\omega t$) with itself, giving the average value of $1/2$.

B Equivalent LTI representation of AFC

An equivalent linear time-invariant (LTI) representation of the AFC controller can be shown to exist. This equivalent representation can be useful in determining stability and robustness properties of the closed-loop system and will be derived here.
The following properties are now defined:

$$\cos(\omega t + \phi) = \frac{1}{2} \left(e^{j\omega t} e^{j\phi} + e^{-j\omega t} e^{-j\phi}\right), \tag{B1}$$

$$\sin(\omega t + \phi) = \frac{1}{2j} \left(e^{j\omega t} e^{j\phi} - e^{-j\omega t} e^{-j\phi}\right), \tag{B2}$$

$$\mathcal{L}\left(x(t) e^{j\omega t} e^{j\phi}\right) = X(s - j\omega) e^{j\phi}. \tag{B3}$$

Using the properties (B1), (B2) and (B3), the new transfer function of the estimated Fourier coefficients is:

$$\begin{aligned}\hat{A}(s) &= \mathcal{L}(\hat{a}(t))\\ &= \mathcal{L}\left(\int 2Ke(t)\cos(\omega t+\phi)dt\right)\\ &= \mathcal{L}\left(\int Ke(t)\left(e^{j\omega t}e^{j\phi}+e^{-j\omega t}e^{-j\phi}\right)dt\right)\\ &= K\frac{1}{s}\left(E(s-j\omega)e^{j\phi}+E(s+j\omega)e^{-j\phi}\right),\end{aligned} \tag{B4}$$

$$\hat{B}(s) = \frac{K}{j}\frac{1}{s}\left(E(s-j\omega)e^{j\phi}-E(s+j\omega)e^{-j\phi}\right). \tag{B5}$$

The transfer function of the control signal is now:

$$\begin{aligned}U(s) &= \mathcal{L}(u(t))\\ &= \mathcal{L}\left(\hat{a}(t)\cos\omega t+\hat{b}(t)\sin\omega t\right)\\ &= \mathcal{L}\left(\hat{a}(t)\frac{1}{2}\left(e^{j\omega t}+e^{-j\omega t}\right)+\hat{b}(t)\frac{1}{2j}\left(e^{j\omega t}e^{j\phi}-e^{-j\omega t}e^{-j\phi}\right)\right)\\ &= \frac{\hat{A}(s-j\omega)+\hat{A}(s+j\omega)}{2}+\frac{\hat{B}(s-j\omega)-\hat{B}(s+j\omega)}{2j}.\end{aligned} \tag{B6}$$

The expressions for $\hat{A}(s-j\omega)$, $\hat{B}(s-j\omega)$, $\hat{A}(s+j\omega)$, $\hat{B}(s+j\omega)$ can be obtained from (B4) and (B5) by substituting $s-j\omega$ (or $s+j\omega$) instead of s:

$$\begin{aligned}\hat{A}(s-j\omega) &= K\frac{1}{s-j\omega}\left(E(s-j2\omega)e^{j\phi}+E(s)e^{-j\phi}\right),\\ \hat{A}(s+j\omega) &= K\frac{1}{s+j\omega}\left(E(s)e^{j\phi}+E(s+j2\omega)e^{-j\phi}\right),\\ \hat{B}(s-j\omega) &= \frac{K}{j}\frac{1}{s-j\omega}\left(E(s-j2\omega)e^{j\phi}+E(s)e^{-j\phi}\right),\\ \hat{B}(s+j\omega) &= \frac{K}{j}\frac{1}{s+j\omega}\left(E(s)e^{j\phi}+E(s+j2\omega)e^{-j\phi}\right).\end{aligned} \tag{B7}$$

Substituting (B7) into (B6) now gives:

$$\begin{aligned}U(s) = &\ \frac{K}{2}\Bigg(\frac{E(s-j2\omega)e^{j\phi}}{s-j\omega}+\frac{E(s)e^{-j\phi}}{s-j\omega}+\frac{E(s)e^{j\phi}}{s+j\omega}+\frac{E(s+j2\omega)e^{-j\phi}}{s+j\omega}\\ &-\frac{E(s-j2\omega)e^{j\phi}}{s-j\omega}+\frac{E(s)e^{-j\phi}}{s-j\omega}+\frac{E(s)e^{j\phi}}{s+j\omega}-\frac{E(s+j2\omega)e^{-j\phi}}{s+j\omega}\Bigg)\\ = &\ K\left(\frac{E(s)e^{-j\phi}}{s-j\omega}+\frac{E(s)e^{j\phi}}{s+j\omega}\right)\\ = &\ K\frac{(s+j\omega)e^{-j\phi}+(s-j\omega)e^{j\phi}}{(s-j\omega)(s+j\omega)}E(s)\\ = &\ K\frac{(s+j\omega)(\cos\phi-j\sin\phi)+(s-j\omega)(\cos\phi+j\sin\phi)}{s^2+\omega^2}E(s)\\ = &\ 2K\frac{s\cos\phi+\omega\sin\phi}{s^2+\omega^2}E(s).\end{aligned} \tag{B8}$$

The resulting LTI transfer function of the controller is now of the following form:

$$C(s) = 2K\frac{s\cos\phi+\omega\sin\phi}{s^2+\omega^2}. \tag{B9}$$

C Sensitivity Transfer Function

In order to inspect the steady-state behaviour of the closed-loop system, the sensitivity function is defined as (refer to the system block diagram in Figure 1b):

$$S(s) = \frac{E(s)}{R(s)} = \frac{1}{1 + P(s)C(s)}, \tag{C1}$$

where $E(s)$ and $R(s)$ are the Laplace transforms of the error and reference signals, respectively, and $C(s)$ is the transfer function of the controller. Considering equation (B9), the controller transfer function can be written, in general, as:

$$C(s) = \frac{A_c(s)}{B_c(s)} = \frac{A_c(s)}{s^2 + \omega^2}, \tag{C2}$$

where ω is the frequency of the reference signal. Combining (C1) and (C2), the sensitivity function can now be expressed as:

$$S(s) = \frac{1}{1 + P(s)\frac{A_c(s)}{B_c(s)}} = \frac{B_c(s)}{B_c(s) + P(s)A_c(s)}. \tag{C3}$$

For $s = j\omega$ the closed-loop transfer function evaluates to:

$$S(j\omega) = \frac{-\omega^2 + \omega^2}{-\omega^2 + \omega^2 + P(s)A_c(s)} = 0, \tag{C4}$$

showing that the steady-state error vanishes and that perfect tracking can be achieved regardless of $P(s)$.

References

[1] P. S. Varoto and L. P. de Oliveira. Interaction between a vibration exciter and the structure under test. *Sound and vibration*, 36 (10):20–26, 2002.

[2] P. Varoto and L. de Oliveira. On the force drop off phenomenon in shaker testing in experimental modal analysis. *Shock and Vibration*, 9:165–175, 11 2002. doi:10.1155/2002/675674.

[3] B. R. Pacini, R. J. Kuether, and D. R. Roettgen. Shaker-structure interaction modeling and analysis for nonlinear force appropriation testing. *Mechanical Systems and Signal Processing*, 162:108000, 2022. ISSN 0888-3270. doi:10.1016/j.ymssp.2021.108000.

[4] G. Tomlinson. Force distortion in resonance testing of structures with electro-dynamic vibration exciters. *Journal of Sound and Vibration*, 63(3):337–350, 1979. ISSN 0022-460X. doi:10.1016/0022-460X(79)90678-3.

[5] M. Peeters, G. Kerschen, and J. Golinval. Modal testing of nonlinear vibrating structures based on nonlinear normal modes: Experimental demonstration. *Mechanical Systems and Signal Processing*, 25(4):1227–1247, 2011. ISSN 0888-3270. doi:10.1016/j.ymssp.2010.11.006.

[6] S. Peter and R. I. Leine. Excitation power quantities in phase resonance testing of nonlinear systems with phase-locked-loop excitation. *Mechanical Systems and Signal Processing*, 96:139–158, 2017. ISSN 0888-3270. doi:10.1016/j.ymssp.2017.04.011.

[7] T.-H. Chen and C.-M. Liaw. Vibration acceleration control of an inverter-fed electrodynamic shaker. *IEEE/ASME Transactions on Mechatronics*, 4(1):60–70, 1999. doi:10.1109/3516.752085.

[8] K. Rana. Fuzzy control of an electrodynamic shaker for automotive and aerospace vibration testing. *Expert Systems with Applications*, 38(9):11335–11346, 2011.

[9] C. Ma, Z. Wu, and C. Yang. *Mechanical Characteristics of Electromagnetic Shakers and its Force Control*. American Institute of Aeronautics and Astronautics, Inc., 2014. doi:10.2514/6.2014-0980.

[10] S. Fukuda and T. Yoda. A novel current-tracking method for active filters based on a sinusoidal internal model [for pwm invertors]. *IEEE Transactions on Industry Applications*, 37(3):888–895, 2001. doi:10.1109/28.924772.

[11] Y. Uchiyama and M. Fujita. Robust control of electrodynamic shaker with disturbance-force compensator. In *2007 European Control Conference (ECC)*, pages 5219–5224, 2007. doi:10.23919/ECC.2007.7068583.

[12] A. Josefsson, M. Magnevall, and K. Ahlin. Control algorithm for sine excitation on nonlinear systems. In *IMAC XXIV*. Society for Experimental Mechanics, 2006.

[13] M. Magnevall, A. Josefsson, and K. Ahlin. Experimental verification of a control algorithm for nonlinear systems. In *IMAC XXIV*. Society for Experimental Mechanics, 2006.

[14] A. Shaw, T. Hill, S. Neild, and M. Friswell. Periodic responses of a structure with 3:1 internal resonance. *Mechanical Systems and Signal Processing*, 81:19–34, 2016. ISSN 0888-3270. doi:10.1016/j.ymssp.2016.03.008.

[15] A. Novak, L. Simon, P. Lotton, and M. Melon. Predistortion technique for generating spectrally clean excitation signals for audio and electro-acoustic nonlinear measurements. In *Audio Engineering Society Convention 146*. Audio Engineering Society, 2019.

[16] G. Abeloos, F. Müller, E. Ferhatoglu, M. Scheel, C. Collette, et al. A consistency analysis of phase-locked-loop testing and control-based continuation for a geometrically nonlinear frictional system. *Mechanical Systems and Signal Processing*, 170: 108820, 2022. ISSN 0888-3270. doi:10.1016/j.ymssp.2022.108820.

[17] P. Hippold, G. Kleyman, L. Woiwode, T. Wei, F. Müller, et al. An iteration-free approach to excitation harmonization. *Mechanical Systems and Signal Processing*, 233:112732, 2025. ISSN 0888-3270. doi:10.1016/j.ymssp.2025.112732.

[18] P. Ioannou and G. Tao. Frequency domain conditions for strictly positive real functions. *IEEE Transactions on Automatic Control*, 32(1):53–54, 1987. doi:10.1109/TAC.1987.1104447.

[19] J. Liu, L. Yang, L. Yang, X. Zhang, and X. Chen. Multiple-harmonic amplitude and phase control method for active noise and vibration reshaping. *Journal of Vibration and Control*, 24(14):3173–3193, 2018.

[20] A. Sacks, M. Bodson, and P. Khosla. Experimental Results of Adaptive Periodic Disturbance Cancellation in a High Performance Magnetic Disk Drive. *Journal of Dynamic Systems, Measurement, and Control*, 118(3):416–424, 09 1996. ISSN 0022-0434. doi:10.1115/1.2801161.

[21] T. Karaağaçlı and H. N. Özgüven. Experimental identification of backbone curves of strongly nonlinear systems by using response-controlled stepped-sine testing (rct). *Vibration*, 3(3):266–280, 2020. ISSN 2571-631X. doi:10.3390/vibration3030019.

[22] M. Scheel, S. Peter, R. I. Leine, and M. Krack. A phase resonance approach for modal testing of structures with nonlinear dissipation. *Journal of Sound and Vibration*, 435:56–73, 2018. ISSN 0022-460X. doi:10.1016/j.jsv.2018.07.010.

[23] F. Müller, L. Woiwode, J. Gross, M. Scheel, and M. Krack. Nonlinear damping quantification from phase-resonant tests under base excitation. *Mechanical Systems and Signal Processing*, 177:109170, 2022. ISSN 0888-3270. doi:10.1016/j.ymssp.2022.109170.

[24] S. Schwarz, L. Kohlmann, A. Hartung, J. Gross, M. Scheel, et al. Validation of a turbine blade component test with frictional contacts by phase-locked-loop and force-controlled measurements. *Journal of Engineering for Gas Turbines and Power*, 142(5): 051006, 03 2020. ISSN 0742-4795. doi:10.1115/1.4044772.

[25] T. Zhou and G. Kerschen. Identification of secondary resonances of nonlinear systems using phase-locked loop testing. *Journal of Sound and Vibration*, 590:118549, 2024. ISSN 0022-460X. doi:10.1016/j.jsv.2024.118549.

[26] P. Hippold, M. Scheel, L. Renson, and M. Krack. Robust and fast backbone tracking via phase-locked loops. *Mechanical Systems and Signal Processing*, 220:111670, 2024. ISSN 0888-3270. doi:10.1016/j.ymssp.2024.111670.

[27] J. Sieber and B. Krauskopf. Control based bifurcation analysis for experiments. *Nonlinear Dynamics*, 51(3):365–377, feb 2008. doi:10.1007/s11071-007-9217-2.

[28] L. Renson, A. Shaw, D. Barton, and S. Neild. Application of control-based continuation to a nonlinear structure with harmonically coupled modes. *Mechanical Systems and Signal Processing*, 120:449–464, 2019. ISSN 0888-3270. doi:10.1016/j.ymssp.2018.10.008.

[29] G. Abeloos, L. Renson, C. Collette, and G. Kerschen. Stepped and swept control-based continuation using adaptive filtering. *Nonlinear Dynamics*, 104(4):3793–3808, jun 2021. doi:10.1007/s11071-021-06506-z.

[30] D. A. Barton, B. P. Mann, and S. G. Burrow. Control-based continuation for investigating nonlinear experiments. *Journal of Vibration and Control*, 18(4):509–520, 2012. doi:10.1177/1077546310384004.

[31] D. A. Barton. Control-based continuation: Bifurcation and stability analysis for physical experiments. *Mechanical Systems and Signal Processing*, 84:54–64, 2017. ISSN 0888-3270. doi:10.1016/j.ymssp.2015.12.039.

[32] L. Renson, A. Gonzalez-Buelga, D. Barton, and S. Neild. Robust identification of backbone curves using control-based continuation. *Journal of Sound and Vibration*, 367:145–158, 2016. ISSN 0022-460X. doi:10.1016/j.jsv.2015.12.035.

[33] J. Sieber, B. Krauskopf, D. Wagg, S. Neild, and A. Gonzalez-Buelga. Control-based continuation of unstable periodic orbits. *Journal of Computational and Nonlinear Dynamics*, 6(1):011005, 09 2010. ISSN 1555-1415. doi:10.1115/1.4002101.

[34] G. Raze, G. Abeloos, and G. Kerschen. Experimental continuation in nonlinear dynamics: recent advances and future challenges. *Nonlinear Dynamics*, 113(6):4949–4997, Mar 2025. ISSN 1573-269X. doi:10.1007/s11071-024-10543-9.

[35] K. Lau, D. Quevedo, B. Vautier, G. Goodwin, and S. Moheimani. Design of modulated and demodulated controllers for flexible structures. *Control Engineering Practice*, 15(3):377–388, 2007. ISSN 0967-0661. doi:10.1016/j.conengprac.2005.09.004. Selected Papers Presented at the Third IFAC Symposium on Mechatronic Systems (2004).

[36] C. Hendrickson and R. T. M'Closkey. Phase Compensation Strategies for Modulated-Demodulated Control With Application to Pulsed Jet Injection. *Journal of Dynamic Systems, Measurement, and Control*, 134(1):011024, 12 2011. ISSN 0022-0434. doi:10.1115/1.4004768.

[37] K. Karvinen and S. Moheimani. Modulated–demodulated control: Q control of an afm microcantilever. *Mechatronics*, 24(6): 661–671, 2014. ISSN 0957-4158. doi:10.1016/j.mechatronics.2013.11.011.

[38] D. Rao and S.-Y. Kung. Adaptive notch filtering for the retrieval of sinusoids in noise. *IEEE Transactions on Acoustics, Speech, and Signal Processing*, 32(4):791–802, 1984. doi:10.1109/TASSP.1984.1164398.

[39] M. Mojiri, M. Karimi-Ghartemani, and A. Bakhshai. Time-domain signal analysis using adaptive notch filter. *IEEE Transactions on Signal Processing*, 55(1):85–93, 2007. doi:10.1109/TSP.2006.885686.

[40] F. F. Costa, R. C. dos Santos, R. R. Ferreira, D. A. Fernandes, L. A. L. de Almeida, et al. Adaptive phasor estimators based on recursive least-squares. In *2013 IEEE Grenoble Conference*, pages 1–6, 2013. doi:10.1109/PTC.2013.6652173.

[41] M. G. Ruppert, K. S. Karvinen, S. L. Wiggins, and S. O. Reza Moheimani. A kalman filter for amplitude estimation in high-speed dynamic mode atomic force microscopy. *IEEE Transactions on Control Systems Technology*, 24(1):276–284, 2016. doi:10.1109/TCST.2015.2435654.

[42] M. Karimi-Ghartemani, S. A. Khajehoddin, P. K. Jain, A. Bakhshai, and M. Mojiri. Addressing dc component in pll and notch filter algorithms. *IEEE Transactions on Power Electronics*, 27(1):78–86, 2011. doi:10.1109/TPEL.2011.2158238.

[43] S. Sastry and M. Bodson. *Adaptive control: stability, convergence and robustness*. Courier Corporation, 2011.

[44] M. F. Byl, S. J. Ludwick, and D. L. Trumper. A loop shaping perspective for tuning controllers with adaptive feedforward cancellation. *Precision Engineering*, 29(1):27–40, 2005. ISSN 0141-6359. doi:10.1016/j.precisioneng.2004.04.005.

[45] S. S. Rao. *Vibration of Continuous Systems*. John Wiley & Sons Ltd, 2007.

[46] G. F. Lang, D. Snyder, et al. Understanding the physics of electrodynamic shaker performance. *Sound and vibration*, 35(10): 24–33, 2001.

[47] N. Tiwari, A. Puri, and A. Saraswat. Lumped parameter modelling and methodology for extraction of model parameters for an electrodynamic shaker. *Journal of Low Frequency Noise, Vibration and Active Control*, 36(2):99–115, 2017. doi:10.1177/0263092317693511.

[48] G. F. Lang. Electrodynamic shaker fundamentals. *Sound and vibration*, 1997.

[49] J. Schoukens, R. Pintelon, E. van der Ouderaa, and J. Renneboog. Survey of excitation signals for fft based signal analyzers. *IEEE Transactions on Instrumentation and Measurement*, 37(3):342–352, 1988. doi:10.1109/19.7453.

[50] G. A. Papagiannopoulos and G. D. Hatzigeorgiou. On the use of the half-power bandwidth method to estimate damping in building structures. *Soil Dynamics and Earthquake Engineering*, 31(7):1075–1079, 2011. ISSN 0267-7261. doi:https://doi.org/10.1016/j.soildyn.2011.02.007.

[51] R. Seydel. *Practical bifurcation and stability analysis*, volume 5. Springer Science & Business Media, 2009.

[52] H. Dankowicz and F. Schilder. *Recipes for continuation*. SIAM, 2013.

[53] D. Shmilovitz. On the definition of total harmonic distortion and its effect on measurement interpretation. *IEEE Transactions on Power Delivery*, 20(1):526–528, 2005. doi:10.1109/TPWRD.2004.839744.

[54] R. Kuether, L. Renson, T. Detroux, C. Grappasonni, G. Kerschen, et al. Nonlinear normal modes, modal interactions and isolated resonance curves. *Journal of Sound and Vibration*, 351:299–310, 2015. ISSN 0022-460X. doi:10.1016/j.jsv.2015.04.035.

[55] A. H. Nayfeh and B. Balachandran. Modal Interactions in Dynamical and Structural Systems. *Applied Mechanics Reviews*, 42 (11S):S175–S201, 11 1989. ISSN 0003-6900. doi:10.1115/1.3152389.

[56] T. Detroux, J.-P. Noël, L. N. Virgin, and G. Kerschen. Experimental study of isolas in nonlinear systems featuring modal interactions. *Plos one*, 13(3):e0194452, 2018.

[57] M. Krack and J. Gross. *Harmonic balance for nonlinear vibration problems*, volume 1. Springer, 2019.

[58] M. Peeters, G. Kerschen, and J. Golinval. Dynamic testing of nonlinear vibrating structures using nonlinear normal modes. *Journal of Sound and Vibration*, 330(3):486–509, 2011. ISSN 0022-460X. doi:10.1016/j.jsv.2010.08.028.

[59] K. B. Ariyur and M. Krstic. *Real-time optimization by extremum-seeking control*. John Wiley & Sons, 2003.

[60] Exciter force control for vibration testing of nonlinear structures using adaptive feedforward cancellation: Supplementary material. 2025, URL `https://dx.doi.org/10.5281/zenodo.17648173`.